



140
052
THS

THESIS
1
2007



This is to certify that the
thesis entitled

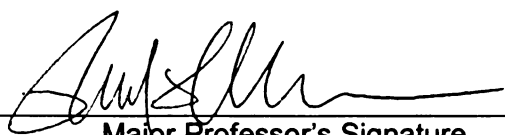
IMPLEMENTATION OF A β -NQR SYSTEM AT THE NSCL
FOR GROUND STATE QUADRUPOLE MOMENT
MEASUREMENTS

presented by

RANKOTHGE R. WEERASIRI

has been accepted towards fulfillment
of the requirements for the

MS degree in Chemistry


Major Professor's Signature

12/22/2006

Date

PLACE IN RETURN BOX to remove this checkout from your record.
TO AVOID FINES return on or before date due.
MAY BE RECALLED with earlier due date if requested.

DATE DUE	DATE DUE	DATE DUE

IMPLEMENTATION OF A β -NQR SYSTEM AT THE NSCL FOR
GROUND STATE QUADRUPOLE MOMENT
MEASUREMENTS

By

Rankothge R. Weerasiri

A THESIS

Submitted to
Michigan State University
in partial fulfillment of the requirements
for the degree of

MASTER OF SCIENCE

Department of Chemistry

2007

ABSTRACT

IMPLEMENTATION OF A β -NQR SYSTEM AT THE NSCL FOR GROUND STATE QUADRUPOLE MOMENT MEASUREMENTS

By

Rankothge R. Weerasiri

The nuclear electric quadrupole moment, Q , is a direct measure of the nuclear charge distribution, and provides an important test of nuclear structure models. The β detected nuclear quadrupole resonance (β -NQR) method is a technique to measure ground state Q of unstable nuclei.

A β -NQR system has been constructed at the NSCL. Several challenges had to be overcome to build the β -NQR system, including the implementation of multi-radio frequencies, high rf magnetic field strength, short rf application time due to the short half-life of exotic nuclei of interest. The new system has four function generators to produce the required rf signals for $I \leq 2$ nuclei. The rf signals are amplified to a maximum of 250 W. After the amplifier, a switched LCR system is used to maximize power delivered to the rf coil. Six variable capacitors, a 50 Ω resistor or impedance matching transformer, and an rf coil represent the complete LCR circuit.

An rf leak test performed on the constructed system showed no significant rf leakage from the high voltage rf box, which holds the resistor, transformer, and variable capacitors. Rf magnetic field strengths were measured to be 18.2 G and 17.6 G for frequencies of 700 ± 10 kHz and 1200 ± 10 kHz, respectively, at maximum power.

First application of the new β -NQR system will be a precision measurement of the Q of ^{37}K . A value 114.7 ± 38.2 mb has been reported in the literature, and a new value with reduced error is important to test the predictions of sd shell model calculations. The Q of ^{35}K will be measured to find evidence for influence of weak proton binding energy in the Q of this very neutron-deficient nucleus.

To
my mother, my family,
all my teachers
and friends

.

ACKNOWLEDGMENTS

I am very grateful to my advisor, Professor Paul F. Mantica, for giving me the opportunity to come to USA and to study at the MSU/NSCL, for his kind and patient supervision, valuable guidance and encouragement during the total time period.

I wish to express my sincere gratitude to Dr. Kei Minamisono, who gave many helpful advice and useful suggestions to fulfill the project successfully.

I thank my guidance committee including Professor Dave Morrissey, Professor Hendrik Schatz and Professor B. Alex Brown for their valuable guidance.

I like to thanks all of my teachers in the Department of Chemistry / MSU and at the NSCL

I would like to acknowledge my thanks to all the present and past members of the beta group at the NSCL including Dr. J. Pereira, Dr. T. J. Mertzimekis, S. N. Liddick, A. D. Davis, B. E. Tomlin, J. Stoker and J. Pinter who gave lot of help and a friendly environment to work.

I also like to thank all the members of Professor Dave Morrissey's group including Chandana Sumiththrachchi who let me to stay in his home when I first came here.

My sincere thanks to all the staff of the NSCL, especially the design group and the electronic group.

Finally, I like to thank Professor Rohini Hewamanna and Professor Pali Mahawatte, University of Colombo, Sri Lanka, who encouraged me to study further.

Contents

1	Introduction	1
1.1	The nuclear electric quadrupole moment	1
1.2	Importance of the quadrupole moment measurements	2
1.3	The quadrupole moment measuring techniques	4
2	β-NQR Methodology	7
2.1	Spin polarization	7
2.2	Implantation of nuclei and preservation of polarization in a host crystal	13
2.3	Hyperfine interactions	13
2.4	NMR search through β -ray asymmetric angular distribution	16
2.4.1	β -ray asymmetric angular distribution	16
2.4.2	Manipulation of spin polarization	18
2.4.3	Depolarization technique	19
2.4.4	Adiabatic fast passage (AFP) technique	19
2.4.5	Extraction of quadrupole moment	21
3	β-NQR Equipment Implementation	25
3.1	Radio frequency generation	27
3.2	RF amplification	30
3.3	LCR circuitry	31
3.4	Rf coil	33
3.5	Stepper motor controlling system	37
3.6	Vacuum relay switching	38
3.7	RPV071 module	44
4	β-NQR system tests	48
4.1	Calibrating of stepper motor controllers for variable capacitor operation	48
4.2	Testing the whole system	49
4.2.1	RF leakage test	49
4.2.2	Cold switching confirmation	49
4.2.3	Low power test	51
4.2.4	Maximum rf field test	52
4.2.5	Capacitance limits on LCR circuit	53

5	β-NQR Application to $^{35,37}\text{K}$	54
5.1	Quadrupole moments of the nuclei in sd shell	54
5.2	Quadrupole moments of potassium isotopes	55
5.3	Quadrupole moment measurement of ^{37}K	57
5.4	Quadrupole moment measurement of ^{35}K	58
5.5	Experimental details	59
6	Summary	62
	<i>Bibliography</i>	65

List of Figures

1.1	Prolate and oblate shapes of nuclear charge distribution	2
2.1	The momentum transfer in a fragmentation reaction.	9
2.2	Schematic representation of yield and polarization curves of fragmentation reaction.	10
2.3	The momentum transfer in a pick-up reaction.	11
2.4	a). Polarization of ^{37}K in KBr and b). ^{37}K ion yield as functions of relative momentum in the proton pick-up reaction.	12
2.5	Energy levels of $I=3/2$ nuclei under magnetic field and magnetic field + electric field gradient.	14
2.6	Definition of the Euler angles for description of the principal axis of the electric field gradient.	17
2.7	Angular distribution of β particles from polarized nuclei.	18
2.8	The motion of nuclear spin under strong static magnetic field and rotating magnetic field	20
2.9	Spin inversion in AFP technique	22
2.10	a) Three frequency sets corresponding to different values of quadrupole coupling constant for a $I = 3/2$ nuclei b) Double ratio vs coupling constant	24
3.1	Schematic representation of the overall β -NQR system	26
3.2	3D drawing of the rf box	28
3.3	Schematic representation of the radio frequency generating system.	29
3.4	Schematic representation of dips in the LCR resonance curve because of gain reduction feature of the rf amplifier.	31
3.5	Schematic representation of a the LCR circuit	32

3.6	3D drawing of the of the rf coil bobbin and the schematic representation of the orientation of the coil bobbin	34
3.7	Inductance of rf coil vs turn number.	36
3.8	Schematic representation of the circuit used to measure the DC character of the rf coil.	36
3.9	Magnetic field strength of the 17/17 coil as a function of direct current.	37
3.10	Schematic representation of stepper motor controlling system	39
3.11	Schematic representation of power supply for motor controllers.	40
3.12	Schematic representation of switch time measuring circuit.	40
3.13	Relay switch response time.	41
3.14	Circuit diagram of relay switch controllers	43
3.15	Relay switch control and rf gate signals	43
3.16	Schematic representation of triggering and timing system	44
3.17	Schematic representation of writing a program to the memory of RPV071.	45
3.18	Schematic representation of a timing program of pulsed-beam depolarization method for $I=3/2$ nuclei	46
3.19	Schematic representation of timing programs of continuous beam depolarization technique and AFP technique for $I=3/2$ nuclei	47
4.1	Switch control signal and rf signal.	50
4.2	LCR resonance frequencies at low power test.	51
4.3	The circuit for the power tests.	52
5.1	Quadrupole moments of $T=1/2$ nuclei in the sd shell.	55
5.2	Quadrupole moments of potassium isotopes.	56
5.3	Partial decay scheme of ^{37}K	57
5.4	Transition frequencies for the quadrupole moment of ^{37}K	58
5.5	Decay scheme of ^{35}K	59
5.6	Transition frequencies of ^{35}K	60
5.7	β -NMR setup at NSCL	61

List of Tables

3.1	Available function generators.	30
3.2	Technical details of the RF amplifier.	31
3.3	Technical details of the vacuum variable capacitors.	32
3.4	Variation of inductance with turn number of rf coils.	35
3.5	Variation of magnetic field strength of the rf coil (17/17) with current.	35
3.6	Node address hardware configuration.	37
3.7	Specifications of relay switches.	38
3.8	Switch response time of relay switches.	41
4.1	Upper and lower limits for stepper motors.	49
4.2	Results of the rf leakage test.	50
4.3	High power tests of the whole system.	53

Chapter 1

Introduction

1.1 The nuclear electric quadrupole moment

The nuclear electric quadrupole moment is a quantity that describes the shape of the nuclear charge distribution. A quadrupole moment of zero indicates a spherically symmetric charge distribution. By convention, the value of the quadrupole moment is taken to be positive for a prolate-shaped charge distribution and negative for an oblate-shaped charge distribution, as shown in Figure 1.1. The electric quadrupole moment operator is given as,

$$eQ = \int \rho(\vec{r}) r^2 (3\cos^2\theta - 1) dv, \quad (1.1)$$

where eQ is the quadrupole moment, $\rho(\vec{r})$ is the charge density, $\vec{r} - (r, \theta, \phi)$ in polar coordinates and dv is the small volume at point r .

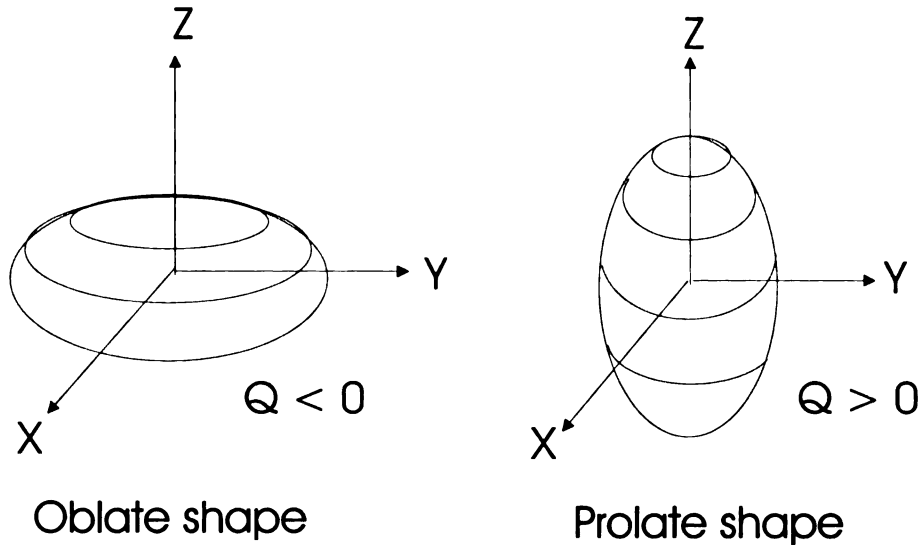


Figure 1.1: Prolate and oblate shapes for non-zero electric quadrupole moment.

1.2 Importance of the quadrupole moment measurements

The quadrupole moment is a valuable tool in the investigation of nuclear structure as it provides detailed information on the spatial distribution of nucleons. For instance, when the proton number Z is near a magic number (eg. $Z=2,8,20,28,- -$ etc), the quadrupole moment changes from plus (one proton below magic number Z) to minus (one proton above magic number Z), suggesting good single-particle states for these nuclei. As an example, the quadrupole moment of ^{39}K ($Z=20-1$) is $+58.5 \pm 6$ mb [1] and the quadrupole moment of ^{41}Sc ($Z=20+1$) is -156 ± 3 mb [2]. The quadrupole moment can indicate the existence of configuration mixing among states like in the deuteron ($^3\text{D}_1$ state mixing with $^3\text{S}_1$ state is compatible with the measured quadrupole moment of 2.8 ± 0.2 mb [3]).

The quadrupole moment is also an indicator of the nuclear core deformation. When the nucleus has a stable core plus one-valence neutron, the single-particle shell model cannot explain a non-zero quadrupole moment, as the neutron is neutral. As an example, the quadrupole moment of ^{17}O with the ^{16}O core and valence neutron in

the $1d_{5/2}$ shell, is -25.78 mb [4]. The presence of a quadrupole moment of ^{17}O can be explained by the core deformation induced by the valence neutron. In the higher-mass region, large quadrupole moments are observed that are several times larger than the single-particle shell model predictions. As an example, the quadrupole moment of $^{204}_{83}\text{Bi}$ is -700 ± 200 mb [2], which contains an even number of neutrons and one odd proton outside the shell closure at $Z=82$. The calculated quadrupole moment using single-particle shell model equations [5],

$$Q_{int} = - \langle r^2 \rangle \left[\frac{2J-1}{2J+2} \right], \quad (1.2)$$

$$Q_{sp} = Q_{int} \left[\frac{J(2J-1)}{(J+1)(2J+3)} \right], \quad (1.3)$$

is 246.4 mb. In equation 1.2 and 1.3, Q_{int} is the intrinsic quadrupole moment, Q_{sp} is the spectroscopic quadrupole moment, r is the nuclear radius and J is the nuclear spin. The intrinsic quadrupole moment is the quadrupole moment of a deformed nucleus whose orientation is fixed in space. However, quantum-mechanically, a deformed nucleus and its orientation are described by a wave function. In a β -NQR experiment, we can measure only the projection of the intrinsic quadrupole moment to the reference axis that is called the spectroscopic quadrupole moment. The enhancement of the experimental quadrupole moment implies large core deformation due to the collective effect of nucleons. The nucleons in the unfilled shells move in a net nuclear potential produced by the core. This potential is not the spherically symmetric one of the shell model, but undergoes deformation. Therefore, even in the ground state, the core is affected by the nucleons in the unfilled shell because of their non-spherically symmetry.

The shape of the nucleus is one of the most important properties in understanding nuclear structure far from the stability line. From the experiments of the interaction cross-section measurements, nuclear matter radii can be determined. However, the nuclear charge radius of ^8B determined by the β -NQR measurement is 20% larger

than the matter radius of 2.45 fm determined from the interaction cross-section measurement [6]. Moreover, the measured quadrupole moment of ^8B by β -NQR method is twice as large as the theoretical value predicted by conventional shell model calculations. This may be a result of the presence of proton halo due to the small proton separation energy (140 keV) as claimed by T. Minamisono *et al.* [6]. However, the Coulomb force among the protons, in opposition to the nuclear force, may prevent the growth of the halo structure and push the protons inside the Coulomb barrier. In addition, the last valence proton of ^8B lies in a $1p_{3/2}$ state and the centrifugal barrier is also against the formation of proton halo. M. Fukuda *et al.* measured the matter radius of ^8B using cross section measurements at projectile energies of 40 MeV/A and 60 MeV/A and proved that it is comparable with the charge radius extracted from the β -NQR measurement [7]. This proves that β -NQR technique could be used as a tool to measure the radial extent of the nuclei.

1.3 The quadrupole moment measuring techniques

The ground state quadrupole moment of exotic nuclei can be obtained using several different techniques. As an example, the quadrupole moment can be deduced from the reduced transition probabilities, $B(E2)$. For even-even nuclei, rotational energy levels are much simpler than in odd-even or odd-odd nuclei. Therefore, even-even nuclei are preferentially used to extract $B(E2)$ values and to deduce the intrinsic quadrupole moment. However, the $B(E2)$ connects two states and extraction of quadrupole moment of a respective state is theory dependent.

Laser spectroscopy is another technique used to measure the quadrupole moment that involves hyperfine interactions of atoms. A laser beam induces transitions among hyperfine levels, which are a result of coupling of electron spin with nuclear spin. The hyperfine magnetic coupling constant (A) and hyperfine quadrupole coupling constant (B), deduced from the resonance laser frequencies, can be used to deduce the magnetic

moment and the quadrupole moment. Restrictions in the laser spectroscopy technique include the desired simple electronic structure of the system and limited available laser frequencies.

Microwave spectroscopy can be applied to measure the quadrupole moment of gas phase molecules. This technique is closely related to laser spectroscopy hyperfine structure measurements. The intensity of the molecular beam should be at least 10^{17} pps to have a good accuracy [8]. Far from the stability line, the production rates of isotopes are well below this limiting value.

Low temperature nuclear orientation is another method to determine the ground state quadrupole moment. Lowering the temperature to the milliKelvin range induces nuclear polarization, from which the quadrupole moment could be extracted from the anisotropic distribution of γ and β rays. In general, the lifetime of the nuclei under investigation should be many minutes or longer, due to the time required to orient the nuclear spin ensemble. For the study of exotic nuclei, lifetimes are typically in the millisecond range.

The method that will be discussed in this thesis is the Beta Nuclear Quadrupole Resonance β -NQR method. It has several advantages over the above-mentioned techniques. In contrast to $B(E2)$ measurements, the β -NQR technique is capable to measure the ground state quadrupole moments of odd-even or odd-odd nuclei with theory independent way. The β -NQR method uses a strong magnetic field that de-couples the electron and nuclear spin that excludes the requirement of simple electronic structure in laser spectroscopy. The β -NQR technique is sensitive to the beam intensities even around 10^1 pps that is about 16 orders of magnitude lower than in microwave spectroscopy. This technique is capable to cope with nuclei having lifetimes as low as 10 ns that is much shorter than the requirement in low temperature nuclear orientation technique.

In addition to the advantages stated above, implementation of β -NQR method at the NSCL is desirable, because the NSCL facility is capable of producing spin po-

larized β emitting nuclei far from the stability line. Low production rates and short lifetimes are the major limitations in the quadrupole moment measurements. The β -NQR technique is one of the best methods to measure quadrupole moment detecting spin polarization by β -ray asymmetry even with those limitations. Another advantage is that it is implemented as an improvement of the present β -NMR system that has successfully measured spin polarization by β -ray asymmetry in several previous experiments. The β -NQR is a technique to measure nuclear electric quadrupole moment of unstable nuclei taking advantage of β -ray asymmetric distribution from spin polarized-nuclei and a detailed explanation is given in chapter 2.

Chapter 2

β -NQR Methodology

The β -ray detected Nuclear Quadrupole Resonance (β -NQR) is a technique to measure nuclear electric quadrupole moments of unstable nuclei taking advantage of the β -ray asymmetric-angular distribution from spin-polarized nuclei. The β -NQR technique has four principle requirements.

1. Nuclear ensemble must be polarized.
2. Polarization must be maintained for the nuclear lifetime.
3. There must be electric quadrupole interactions to observe the quadrupole moment.
4. Destruction of polarization by applied radio frequency (rf) magnetic field.

Each requirement will be explained in detail in the following sections.

2.1 Spin polarization

The nuclear spin polarization is one of the major requirements of the β -NQR technique. The nuclear spin is a result of the coupling of intrinsic spin of the nucleons to the orbital angular momentum of nucleons. The nuclear spins are, in general, randomly oriented. Therefore a sample of nuclei has zero net spin orientation. However, if the nuclear spins are preferentially oriented relative to some external reference, the

nuclei are said to be spin polarized. In quantum mechanics, the spin polarization can be considered as a linear distribution of population in magnetic sub-states given by equation,

$$P = \Sigma m a_m / I, \quad (2.1)$$

where P is the nuclear polarization, m is the magnetic quantum number, a_m is the population of magnetic sub-state m and I is the nuclear spin.

Low temperature nuclear orientation, laser optical pumping, nuclear reactions, etc., can generate polarization. In this thesis, production of polarization by intermediate-energy nuclear reactions is considered. In projectile fragmentation, nucleons in the overlap region of the target and the projectile are removed and the remaining part of the projectile moves as the projectile-like fragment with almost the same velocity of the incident projectile. In this process, which is essentially peripheral, momentum is carried away by the removed part and as a result the projectile-like fragment gains an angular momentum L , which leads to the spin polarization of the projectile-like fragment as shown in figure 2.1. According to the experiment done by Asahi *et al*, the magnitude and the sign of the polarization change from low momentum to high momentum [9] relative to the central momentum of the projectile-like fragment shown in figure 2.2. By convention, the polarization is positive when the spin is parallel to the vector $\vec{p}_0 \times \vec{p}$, where \vec{p}_0 is the momentum of projectile and \vec{p} is the momentum of projectile-like fragment. One of the important features of polarization induced by fragmentation is that zero polarization at the peak of the yield curve, and higher polarization where the yield is low. Therefore, low counting rates are expected in the polarization measurements.

In the intermediate-energy regime ($E/A = 20 - 200$ MeV), the nucleon pick-up reaction has a significant contribution [10], specifically when the mass of the projectile is close to the mass of the projectile-like fragment. In a pick-up reaction, a target nucleon is preferentially picked up when that nucleon has the Fermi momentum and is

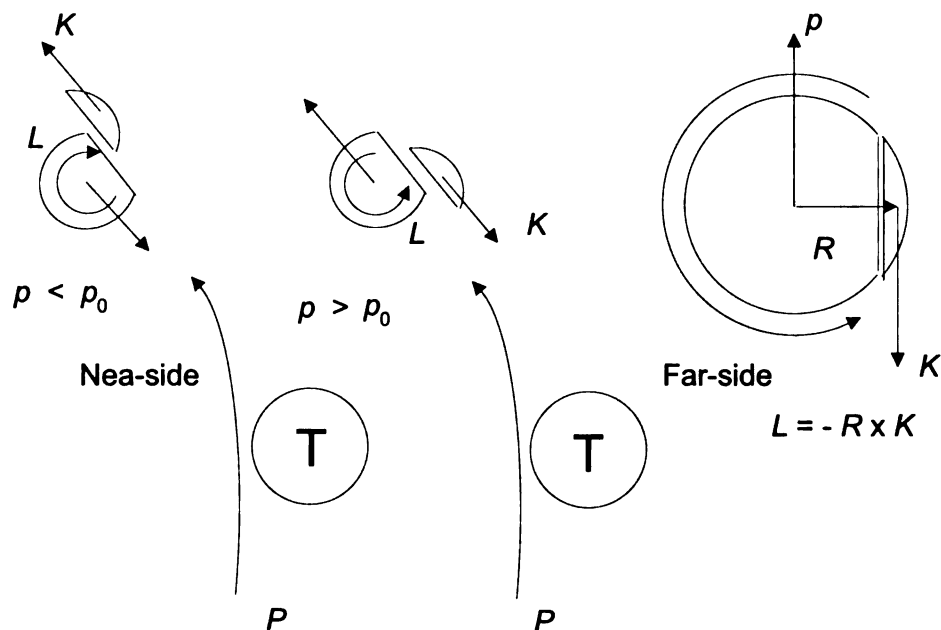


Figure 2.1: The momentum transfer in a fragmentation reaction in the case of a Coulomb dominant near-side collision [9]. Here, p_0 is the momentum of the incident projectile, p is the momentum of the projectile-like fragment, R is the vector pointing from the projectile-like fragment to the removed portion, L is the angular momentum gained by the projectile-like fragment and K is the momentum of the removed portion in the projectile rest frame.

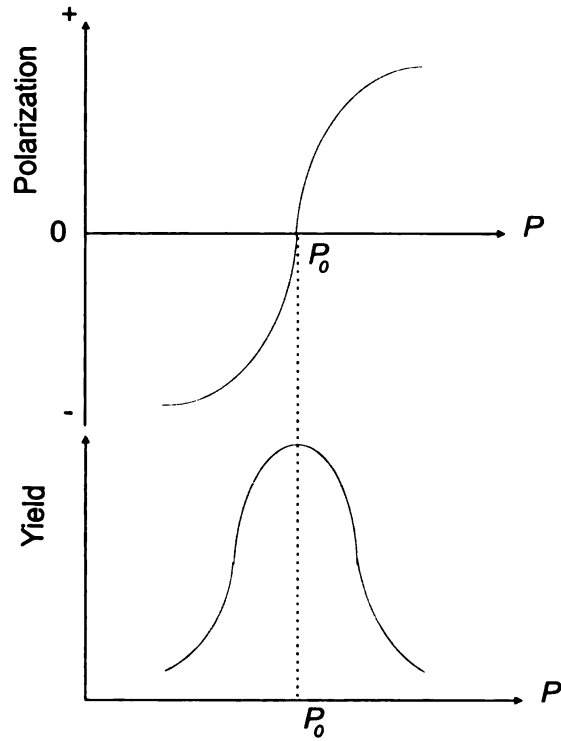


Figure 2.2: Schematic representation of yield and polarization curves of fragmentation reaction in the case of near-side collision with a heavy target [9]. Zero polarization is observed at the peak of the momentum yield curve and the sign of the polarization changes from low momentum to high momentum relative to central momentum of projectile-like fragments.

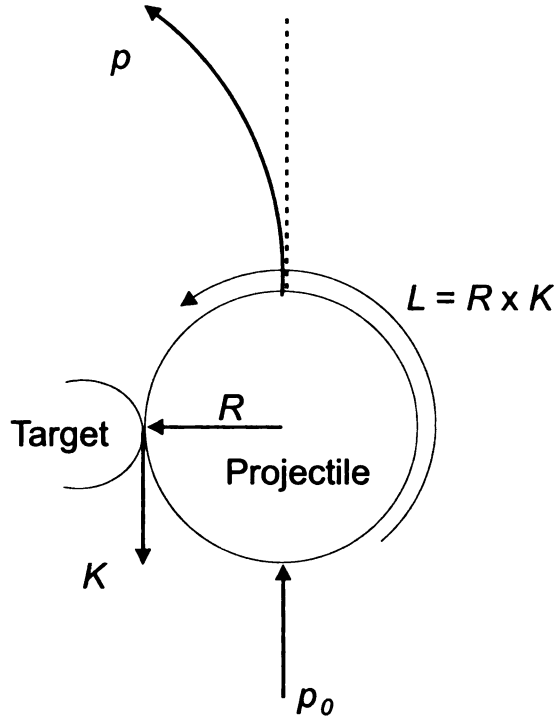


Figure 2.3: The momentum transfer in a pick-up reaction in the case of attractive far side collision in a light target [11]. Here, p_0 is the momentum of the incident projectile, p is the momentum of the projectile-like fragment, R is the vector pointing the position of the picked-up nucleon, L is the angular momentum gained by the projectile-like fragment and K is the linear momentum of the picked-up nucleon in the projectile rest frame.

aligned along with the direction of momentum of the incident projectile [10]. The pick-up reaction is also a result of a peripheral collision. The picked up nucleon introduces an angular momentum to the projectile as shown in figure 2.3 because of velocity difference between the picked up nucleon and the projectile. When the primary beam momentum is comparatively higher than the Fermi momentum, significant spin polarization can be expected from the pick-up reaction [11]. In the pick-up reaction, the highest polarization occurs around the peak of the momentum yield curve as given in figure 2.4.

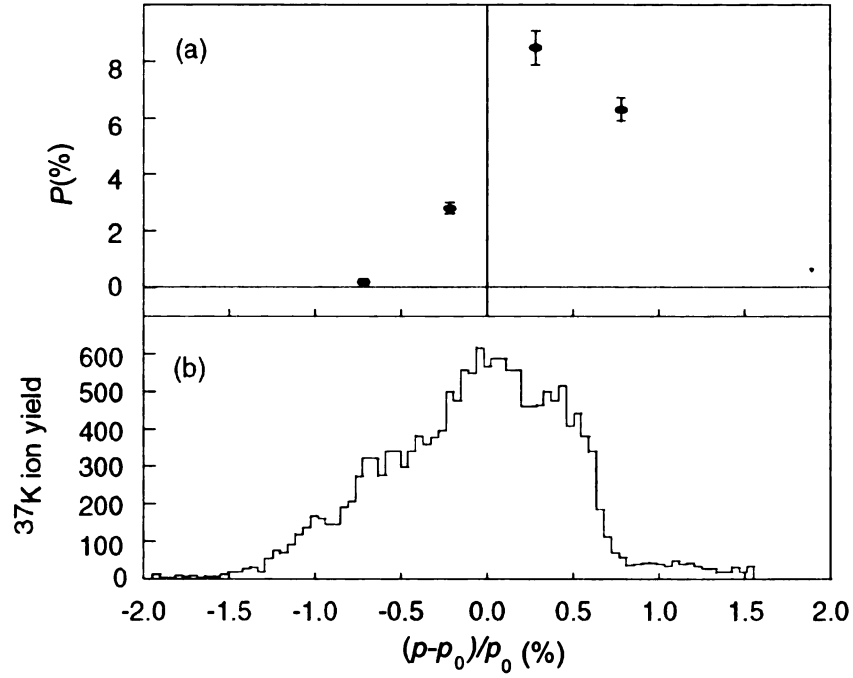


Figure 2.4: a) Polarization of ^{37}K and b) ^{37}K ion yield as functions of momentum of ^{37}K to the central momentum of ^{37}K [11]. ^{37}K is produced by the proton pick-up reaction of $^{36}\text{Ar} + p \rightarrow ^{37}\text{K}$ with a beam energy of 150 MeV/A and implanted in a KBr single crystal. Maximum polarization occurs near the peak of the yield curve.

2.2 Implantation of nuclei and preservation of polarization in a host crystal

Polarized nuclei are implanted in a host crystal, which has an electric field gradient. In the β -NQR technique, the polarization is measured by the angular distribution of β particles. Therefore, polarization has to be preserved until the β decay occurs. Depolarization occurs due to two main processes: spin-lattice relaxation and spin-spin relaxation. Spin-lattice relaxation or longitudinal relaxation is a result of interaction between nuclear spin with the surrounding crystal lattice that is characterized by the spin-lattice relaxation time T_1 . In the process of spin-spin relaxation, or transverse relaxation, polarization is destroyed due to the interaction between opposite spins. This process is characterized by spin-spin relaxation time T_2 . The spin polarization is preserved with the help of a strong external magnetic field H_0 and symmetric environment in the crystal. In addition, the strong magnetic field is helpful to avoid the possible reduction of the polarization through coupling between the nucleus and the orbital electrons during its flight from the final degrader to the host crystal. The strong magnetic field prevents the coupling of the nuclear moments with the fluctuating electromagnetic fields produced by the radiation damages during the implantation process into the crystal.

2.3 Hyperfine interactions

In the presence of a strong magnetic field H_0 , a nuclear spin energy level breaks degeneracy into several magnetic sub-states (Zeeman splitting) represented by the magnetic quantum number as shown in figure 2.5. The energy of the magnetic state, E_m , is given as,

$$E_m = -mg\mu_N H_0 = h\nu, \quad (2.2)$$

Ex :- $I = 3/2$

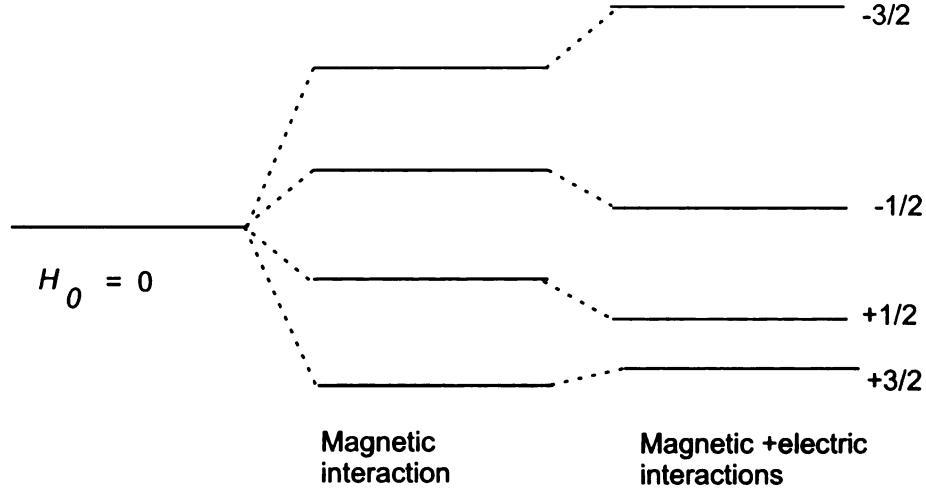


Figure 2.5: Energy levels of $I=3/2$ nuclei under magnetic field and magnetic field + electric field gradient. In the presence of magnetic field energy level splitting have equal spacing however under the influence of electric field energy spacing become uneven.

where g is the nuclear g -factor, ν is the frequency corresponds to the energy E_m , h is the Plank constant and μ_N is the nuclear magneton. The transition frequency, which corresponds to the energy difference between any adjacent magnetic sub-state is called the Larmor frequency, ν_L . In β -NQR experiments, a host crystal is used with an electric field gradient given as,

$$V_{ii} = \frac{d^2V}{di^2}, \quad (2.3)$$

here, V_{ii} is the electric field gradient along i^{th} -axis in the crystal and V is the electrostatic potential in the crystal. The electric interaction shifts the energy levels from the Zeeman splitting as shown in figure 2.5, because of the interaction between the quadrupole moment and the electric field gradient. The largest component of the electric field gradient eq and the asymmetry parameter η of the crystal are defined as,

$$\eta = \frac{V_{xx} - V_{yy}}{V_{zz}}, \quad |V_{xx}| < |V_{yy}| < |V_{zz}|, \quad eq = V_{zz}. \quad (2.4)$$

The Hamiltonian for magnetic and electric interactions is given by, 2.5,

$$H = H_M + H_Q$$

$$= -I_z g \mu_N H_0 + \frac{e^2 q Q}{h} \frac{h}{4I(2I-1)} [3I_z^2 - I(I+1) + \frac{1}{2}\eta(I_+^2 + I_-^2)], \quad (2.5)$$

where, Q is the electric quadrupole moment, e is the electronic charge, I is the nuclear spin, I_z is the third component of nuclear spin operator, I_+, I_- are the raising and lowering operators and θ and ϕ are the rotating angles around z and Y axis respectively. If the quantization axis is selected parallel to the external magnetic field H_0 , the electric part of the Hamiltonian (second term in equation 2.5) can be re-written, using the Euler angle defined in figure 2.6, as,

$$H_Q = \frac{e^2 q Q}{h} \frac{h}{4I(2I-1)} \left[\frac{1}{2}(3\cos^2\theta - 1) + \left(\frac{\eta}{2}\sin^2\theta \cos 2\phi\right)(3I_z^2 - I(I+1)) \right.$$

$$+ \left(\frac{3}{4}\sin 2\theta - \frac{\eta}{4}\sin 2\theta \cos 2\phi + i\frac{\eta}{2}\sin\theta \sin 2\phi\right)(I_+ I_z + I_z I_+)$$

$$+ \left(\frac{3}{4}\sin 2\theta - \frac{\eta}{4}\sin 2\theta \cos 2\phi - i\frac{\eta}{2}\sin\theta \sin 2\phi\right)(I_- I_z + I_z I_-)$$

$$+ \left(\frac{3}{4}\sin^2\theta + \frac{\eta}{4}(\cos^2\theta + 1)\cos 2\phi - i\frac{\eta}{2}\sin\theta \sin 2\phi\right)I_+^2$$

$$\left. + \left(\frac{3}{4}\sin^2\theta + \frac{\eta}{4}(\cos^2\theta + 1)\cos 2\phi + i\frac{\eta}{2}\sin\theta \sin 2\phi\right)I_-^2 \right] \quad (2.6)$$

When the electric interaction is weaker than the magnetic interaction, the electric part of the Hamiltonian H_Q can be considered as a perturbation to the magnetic part of the Hamiltonian H_M . In the first-order perturbation calculation, the energy levels E_m are given as,

$$E_m = -mg\mu_N H_0 + \frac{e^2 q Q}{4I(2I-1)} \left[\frac{3\cos^2\theta - 1}{2} + \frac{\eta \sin^2\theta \cos 2\phi}{2} \right] [3m^2 - I(I+1)] \quad (2.7)$$

Because of m^2 dependence, the m states are not equally split as shown in figure 2.5.

The transition frequency $\nu_{(m \leftrightarrow m-1)}$ between two adjacent magnetic states is given

as,

$$\nu_{(m \leftrightarrow m-1)} = \frac{g\mu_N H_0}{h} + \frac{e^2 q Q}{h} \frac{3}{4I(2I-1)} \left[\frac{3 \cos^2 \theta - 1}{2} + \frac{\eta \sin^2 \theta \cos 2\phi}{2} \right] [1 - 2m]. \quad (2.8)$$

As an example, in the case of $I=3/2$, three resonance frequencies are $\nu_L - \nu_Q$, ν_L and $\nu_L + \nu_Q$ with $\theta=0$ and $\eta=0$ and the split between highest and lowest transition frequencies equals twice quadrupole coupling constant $2\nu_Q$.

$$\nu_Q = \frac{3e^2 q Q}{2hI(2I-1)} \quad (2.9)$$

2.4 NMR search through β -ray asymmetric angular distribution

2.4.1 β -ray asymmetric angular distribution

β decay is caused by the weak interaction which violates parity conservation [12]. Therefore, the angular distribution of β -particle emission is not symmetric relative to the polarization direction as shown in figure 2.7, where β -rays are detected by placing two sets of β -ray detectors at 0° (up) and 180° (down). The angular distribution of β emission is given by equation,

$$N(\theta) \sim 1 + AP \cos \theta, \quad (2.10)$$

where, $N(\theta)$ is the number of β particles detected at an angle θ between the direction of β -ray and polarization P and A is the asymmetry parameter. The magnetic sub-state energy levels can be examined by inducing a polarization change that is detected by a change of $N(\theta)$. The magnetic sub-state energy levels are related to the nuclear

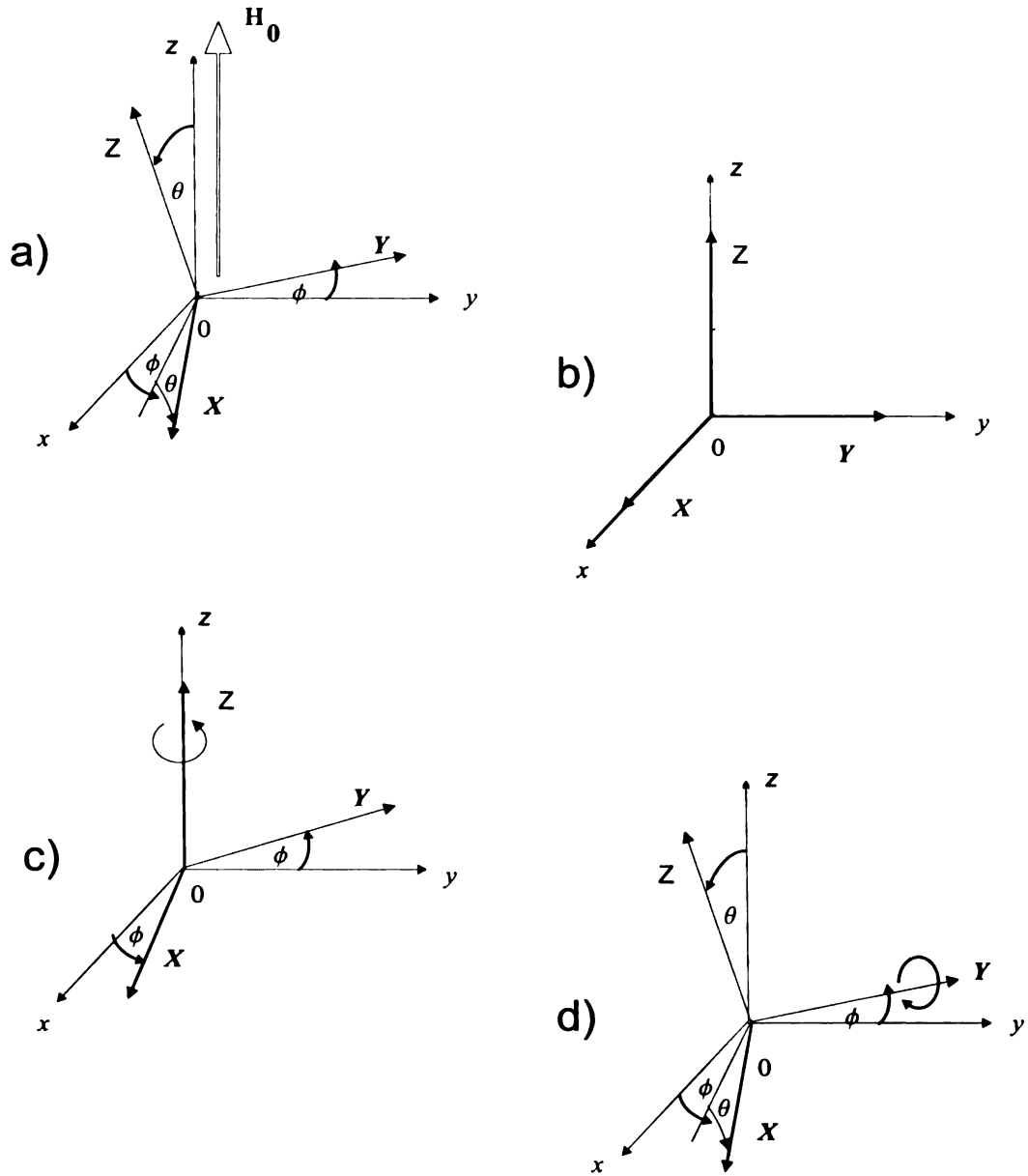


Figure 2.6: a). Definition of the Euler angles for description of the axis of the electric field gradient where X, Y and Z are the coordinate of the crystal and x, y and z are the coordinate in a lab frame. b-d). And its detailed circumstances of rotation from the $\theta = \phi = 0$ state where θ is the angle between Z and z axis and ϕ is the angle between Y and y axis.

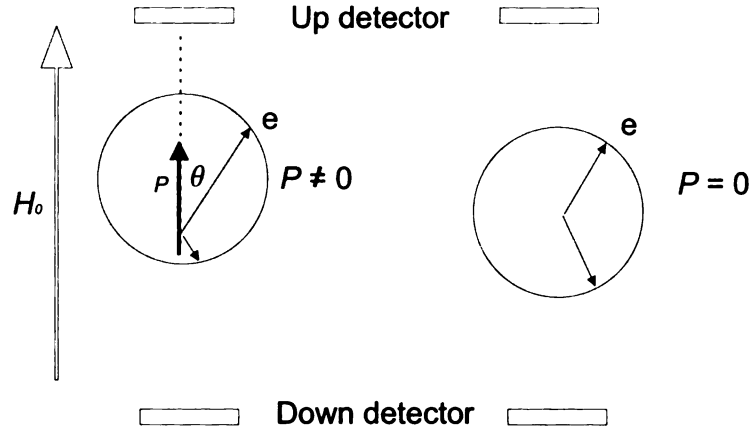


Figure 2.7: Angular distribution of β particles from polarized nuclei. β emission is isotropic in the absence of polarization and it becomes asymmetric in the presence of polarization in an external magnetic field.

magnetic and electric moments and this point is discussed in the next section.

2.4.2 Manipulation of spin polarization

The spin polarization can be considered as a linear distribution of population among magnetic sub-states as given in equation 2.1. Radio frequency (rf) is used to manipulate the spin polarization by inducing transitions between two adjacent magnetic sub-states. This leads to an equilibrium of the magnetic state populations. In the presence of strong magnetic field and without electric field gradient, only one transition frequency, The Larmor frequency, is required for spin depolarization. However, in the quadrupole moment measurement, several transition frequencies are required to manipulate the population among energy levels, as the energy gaps are not equal as discussed in section 2.3. The difference of the polarization before and after the depolarization is a measurable property that is discussed later. There are two main methods to manipulate the spin polarization with rf: depolarization and AFP techniques.

2.4.3 Depolarization technique

In the presence of a strong magnetic field H_0 , spin precesses around the field axis at an angular frequency ω_0 . The equation of motion for spin precession is given as,

$$\frac{\partial \vec{I}}{\partial t} = \gamma h \vec{I} \times \vec{H}_0, \quad (2.11)$$

where γ is the gyro-magnetic ratio. For NMR, an rf magnetic field H_1 , which rotates at angular frequency ω_1 , is applied perpendicular to the H_0 as shown in figure 2.8. In the rotating frame of H_1 , nuclear spin feels effective magnetic field H_{eff} and precesses around H_{eff} as shown in figure 2.8 b),

$$\frac{\partial \vec{I}}{\partial t} = \gamma h \vec{I} \times [\vec{H}_0 + \frac{\vec{\omega}_1}{\gamma} + \vec{H}_1] \quad H_{eff} = [\vec{H}_0 + \frac{\vec{\omega}_1}{\gamma} + \vec{H}_1]. \quad (2.12)$$

At the resonance, ω_1/γ is equal to H_0 and H_1 is equal to H_{eff} . As a result, the spin precesses around the $H_{eff} = H_1$ that is perpendicular to H_0 as given in figure 2.8 c) and as given in equation,

$$\frac{\partial \vec{I}}{\partial t} = \gamma h \vec{I} \times \vec{H}_1. \quad (2.13)$$

Due to time averaging, the spin expectation value along the z-axis I_z becomes zero. Therefore, spin polarization vanishes as it is defined as the expectation value of the z-component I_z of the spin normalized by the total spin I as given in equation,

$$P = \frac{\langle I_z \rangle}{I}. \quad (2.14)$$

2.4.4 Adiabatic fast passage (AFP) technique

In this technique, the rf is swept once over the resonance frequency that results in an inversion of the population between two adjacent magnetic sub-states. Two adiabatic conditions have to be fulfilled to achieve efficient AFP process. Firstly, the rf magnetic

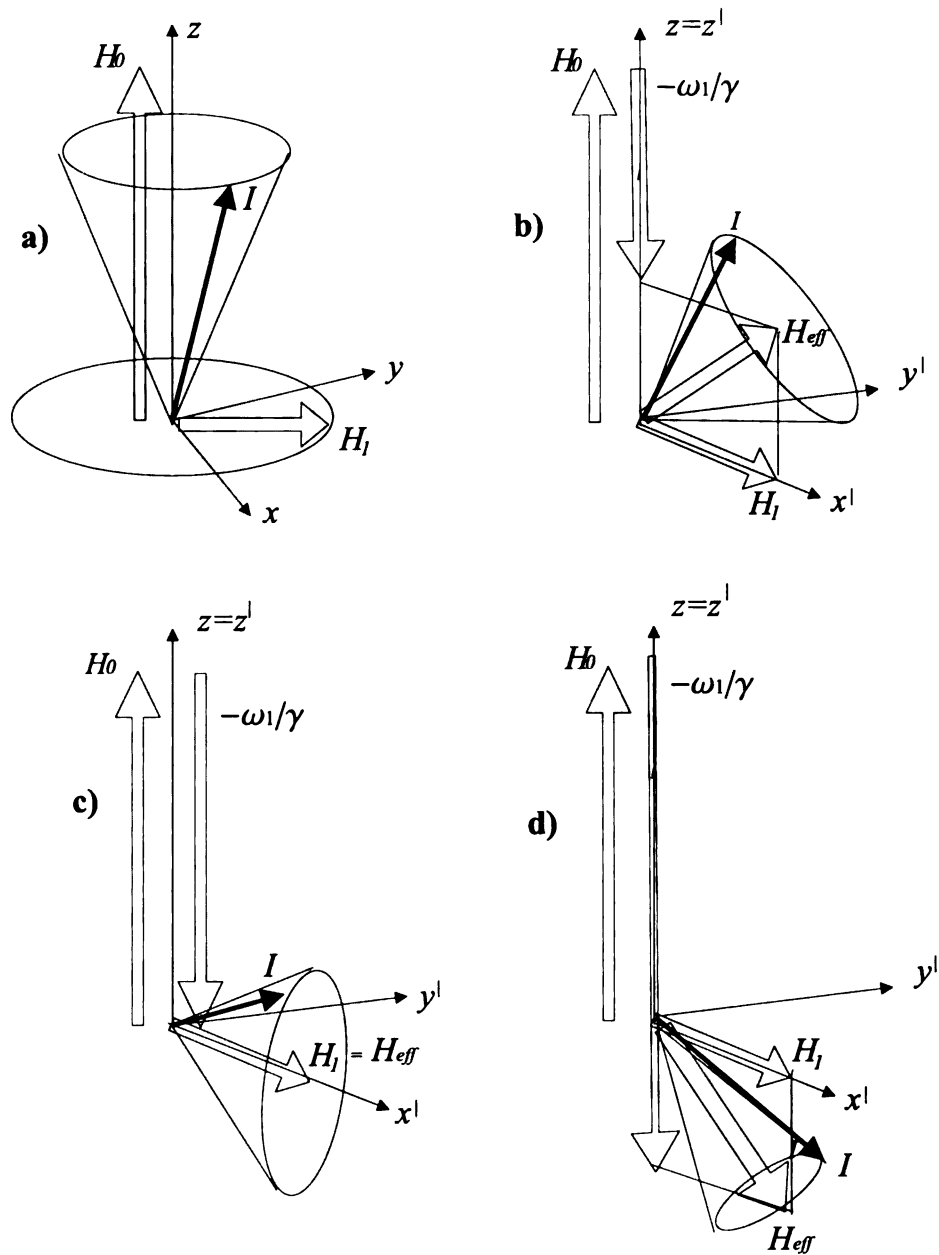


Figure 2.8: The motion of nuclear spin under strong static magnetic field and rotating magnetic field, here x, y, z are coordinates in lab frame and x', y', z' are coordinates in rotating frame. a). Spin precession around the strong external magnetic field b). Spin precession around the effective magnetic field in the rotating frame of H_1 c). Spin precession around the $H_1 = H_{eff}$ at resonance. d). Spin inversion in AFP process

field strength H_1 and frequency sweeping speed should satisfy the first condition given as,

$$(\gamma_N H_1)^2 \gg \left| \frac{d\omega}{dt} \right|, \quad (2.15)$$

where $d\omega$ is the frequency modulation and dt is the frequency modulation time. Secondly, H_1 must be stronger than the local field H_L at the nucleus given as,

$$\gamma H_1 \gg \gamma H_L. \quad (2.16)$$

According to the relationship in 2.15, the sweeping speed should be less than the angular velocity of spin precession around H_{eff} so that the spin follows the change of the effective magnetic field. In addition, according to the relationship in 2.16, the rf magnetic field should be strong enough to prevent any coupling of the nuclear spins with local fields. When there is a static magnetic field and perpendicular rf magnetic field, the spin precesses around the effective field as explained in previous section. Under the adiabatic conditions when the frequency is swept once, the direction of the effective magnetic field is inverted. As a result, the bulk spin is also inverted as shown in figure 2.8 d). Spin inversion makes the NMR signal two times larger than that in depolarization technique as explain in the next section. However, higher rf magnetic field strengths are required to satisfy the AFP condition compared with depolarization technique. In the β -NQR technique, spin inversion needs several applied frequencies in sequence. As an example for a $I=3/2$ nuclei, three transition frequencies rf1, rf2 and rf3 are required. Three frequencies have to be applied in a sequence of 1,2,3,1,2,1 as shown in figure 2.9 in details.

2.4.5 Extraction of quadrupole moment

The quadrupole moment is extracted from the change of the spin polarization during the rf spin manipulation. In the depolarization technique, the ratio between up and

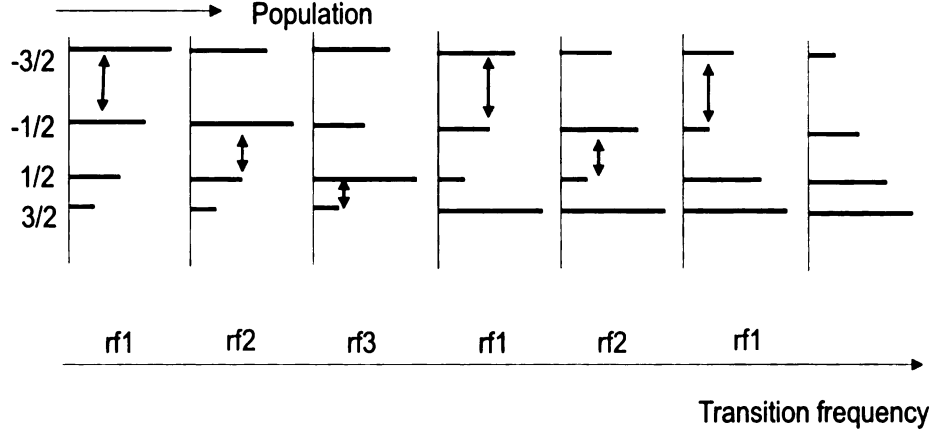


Figure 2.9: In the case of $I=3/2$, spin inversion in AFP technique. Rf1 inverts the population between magnetic state $-3/2$ and $-1/2$ and rf2 inverts the population between $-1/2$ and $1/2$ states and so on. Total inversion of population occurs after applying the sequence of rf1, rf2, rf3, rf1, rf2 and rf1.

down counters is calculated for both rf field on (R_{on}) and off (R_{off}),

$$R_{off} = g_f \frac{1 + AP_0}{1 - AP_0} \quad R_{on} = g_f \frac{1 + AP_1}{1 - AP_1}. \quad (2.17)$$

The difference $\Delta P = P_0 - P_1$ reflects the change in the magnetic sub-state population distributed to the rf excitation, the geometrical factor, g_f , is attributed to the imperfect symmetry of the experimental setup, for example, slight changes of efficiencies of up and down counters. The geometrical factor is cancelled when the double ratio is calculated as given in equation,

$$R_D = \frac{R_{off}}{R_{on}} \approx 1 + 2A(P_0 - P_1) = 1 + 2A\Delta P. \quad (2.18)$$

The obtained signal R_D is maximum when ΔP is maximum ($\Delta P = P_0$ with $P_1 = 0$). In the AFP technique, the double ratio gives twice as large an asymmetry change than in depolarization technique as shown in equations,

$$R_{off} = g_f \frac{1 + AP_0}{1 - AP_0} \quad R_{on} = g_f \frac{1 - AP_0}{1 + AP_0}, \quad (2.19)$$

$$R_D = \frac{R_{off}}{R_{on}} \approx 1 + 4AP_0. \quad (2.20)$$

One of the most important features in the quadrupole moment measurement is that several transition frequencies are needed to manipulate the population among energy levels, as energy gaps between adjacent m states are not equal to each other as discussed in section 2.3. In depolarization technique, one resonance frequency equalizes population between two adjacent magnetic sub-states and reduces the spin polarization partially resulting in a small polarization change ΔP and hence small R_D . For $I=3/2$, the partial depolarization with one resonance frequency leads to only a 10% change of total asymmetry ($A\Delta P$) and it needs hundred times more counting time to reach the same statistics as in full depolarization, since the required time to reach certain statistics is proportional to the figure of merit, $1/P^2Y$, where Y is the yield. These facts strongly indicate the importance of the total depolarization for a reliable and an efficient measurement.

For $I=3/2$, the transition frequencies are calculated from equation 2.8 given in sub-section 2.3, as a function of eqQ/h , and a set of three frequencies are applied simultaneously. As discussed before, the split of highest and lowest transition frequencies is proportional to ν_Q . If the R_D is measured as a function of the electric quadrupole-coupling constant ν_Q , at the true coupling constant there is resonance as shown in figure 2.10. With the known electric field gradient of the host crystal, the electric quadrupole moment can be extracted. For the extraction of quadrupole moments are needed coupling constants of different isotopes measured in the same crystal where one of the quadrupole moments is known,

$$\frac{X_{known}}{X_{unknown}} = \frac{Q_{known}}{Q_{unknown}}. \quad (2.21)$$

Here, X represents the experimentally measured coupling constants.

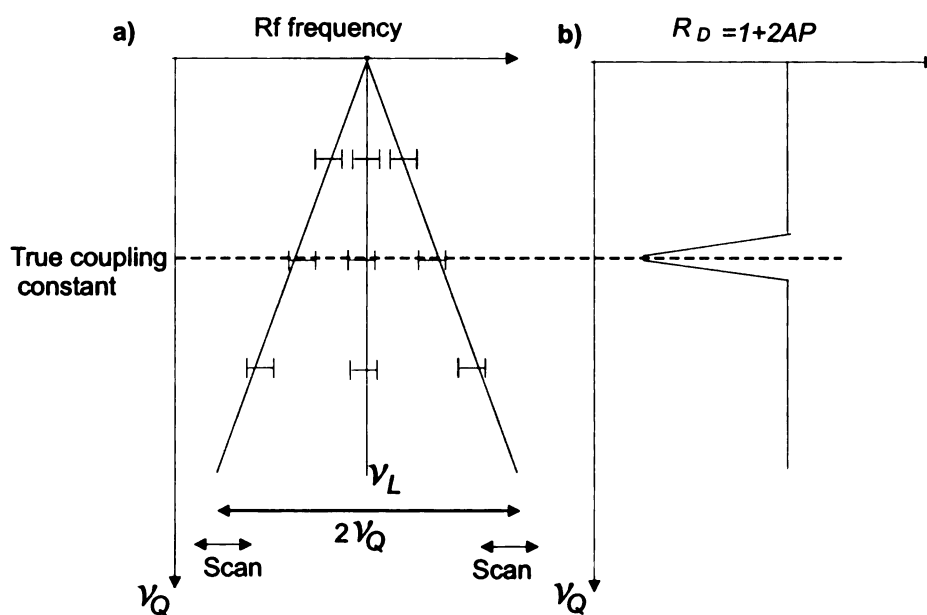


Figure 2.10: a). Three frequency sets corresponding to different values of quadrupole coupling constant for a $I = 3/2$ nuclei. b). Double ratio vs coupling constant. When correct set of frequencies are applied which corresponds to the true coupling constant, significant change of R_D can be observed.

Chapter 3

β -NQR Equipment Implementation

A β -NQR system is being implemented as an upgrade of the β -NMR system at the NSCL with its β -NMR technique capabilities left intact. The β -NQR system can be more efficient to perform β -NMR measurements as well. During the upgrade, several important points were taken into consideration as summarized in the following section. In a magnetic moment measurement with the β -NMR technique, only one transition frequency is needed because the spacings are equal among the nuclear magnetic sub-state energy levels under a strong external magnetic field. On the other hand, in a quadrupole moment measurement with β -NQR technique, those spacings become uneven as a result of the electric interactions introduced in the magnetically interacting systems as explained in chapter 2. Therefore, the β -NQR system must handle several different transition frequencies in sequences or almost simultaneously in order to efficiently equalize or inverse the population of the magnetic sub-states. Application of multiple-frequency NMR requires fast switching among these different transition frequencies because the exotic nuclei of interest have very short life-times (in millisecond range). Also, a high radio frequency (rf) magnetic field strength is one of the important requirements for efficient measurements in both β -NMR and β -NQR techniques, especially when the AFP technique is performed. A significant current should flow through the rf coil to exert a high magnetic field ($> 10\text{G}$), which

relevant to specific electric coupling constant. A pulse pattern generator, RPY071, triggers the function generators in sequence. Each rf signal is gated using the same signal that triggers the function generator. After gating, the rf signal goes to a 250 W rf amplifier and then to a LCR resonance circuit. A 50 Ω resistor or a transformer fulfill the impedance matching between the amplifier and the rf coil. A 50 Ω resistor, six variable capacitors and an rf coil make up virtually six independent LCR circuits. The variable capacitors are controlled to tune the circuit to a specific frequency by stepper motors, which are remotely controlled by stepper motor drivers. Relay switches are used to select one of the LCR circuit out of six, depending on the transition frequency. These relay switches are remotely controlled by a switch driver system to which TTL control signals are sent by the RPY071 pulse pattern generators. An rf box contains the impedance matching transformer, a 50 Ω resistor, six variable capacitors, six relay switches, six relay switch drivers and a DC power supply for the switch drivers as shown in figure 3.2. The rf coil, which produces rf magnetic field for NMR, is placed in the vacuum chamber in the middle of the NMR magnet. The rf coil and the rf box are connected by a coaxial 50 Ω cable. Each component will be explained in detail in the following sections.

3.1 Radio frequency generation

Four different radio frequencies can be handled in the present system using four function generators manufactured by Agilent Technologies. Some technical details of the function generators are given in the table 3.1. The function generators can be triggered internally or externally using TTL logic signal to start a linear frequency sweep. The rf signals are gated by a module (X2M-01-411B / Pulser Corporation) using trigger signals from RPY071. The rf signals from different function generators are gathered to one path by a logic OR gate (433A / ORTEC) and sent to a 250 W amplifier. The overall representation of the radio frequency generation and related

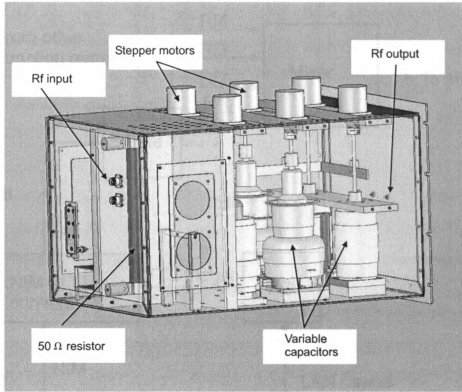


Figure 3.2: 3D drawing of the rf box.

instruments are shown in figure 3.3. The 33220A function generators have LAN ports and are assigned their own IP address. The 33250A function generator has a serial port, which is connected to a device server (USB 10 / LANTRONIX) with a LAN port and IP address. A program, 33220A.tcl, written in Tcl script is used to control the device. In the control program, the carrier frequency, the amplitude of output voltage, Sweep or FM mode, frequency modulation range and modulation time are specified. In sweep mode, the function generator steps the specified frequency region by changing the frequency every 40 ns. Thus, the sweep time determines the sweep frequency resolution. In FM mode, the step is much finer than that in sweep mode. Selecting a trigger mode from IMM or EXT, an internal triggering or an external triggering can be activated, respectively. In FM mode, only IMM trigger can be selected. For the depolarization, sweep mode or FM mode and IMM trigger should be used and for AFP, sweep mode and EXT trigger has to be used.

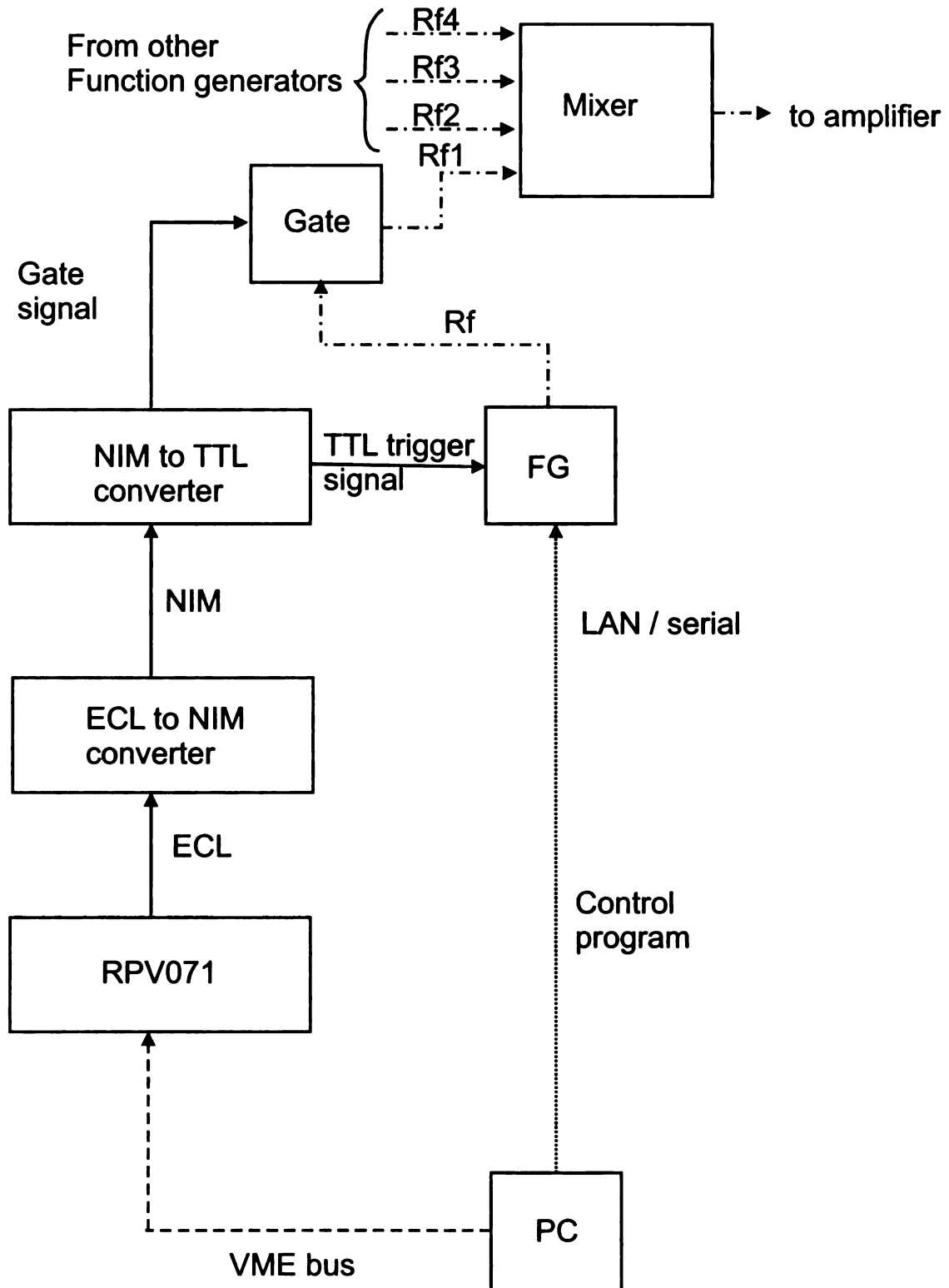


Figure 3.3: Schematic representation of radio frequency generating system. Four function generators are triggered by RPV071 and one rf signal out of four is selected by the same gate signal as the one used for function generator triggering.

Table 3.1: Available function generators. Four function generators are used in the system, which manufactured by Agilent Technologies. Three of them can generate rf up to 20 MHz and one can generate rf up to 80 MHz.

Type	33250A	33220A
Quantity	1	3
Frequency range	1 μ Hz - 80 MHz	1 μ Hz - 20 MHz
Amplitude	10 mVpp - 10 Vpp	10 mVpp - 10 Vpp
FM frequency range	2 mHz - 20 kHz	2 mHz - 20 kHz
Sweep time	1 ms - 500 s	1 ms - 500 s
Control singal via	Serial (RS232)	LAN
Output impedance	50 Ω	50 Ω

3.2 RF amplification

In order to obtain a rough idea of the NMR resonance frequency at an early stage of an experiment, a wide frequency modulation is useful to cover wider search area. This requires a high rf power since the resonance-line width is finite, <10 kHz in general. Also, for the AFP technique, a larger rf power is required that in the depolarization technique as discussed in the sub-section 2.4.4. In the present system, a 250 W rf amplifier is used, which was manufactured by EMPowr RF Systems and capable of amplifying signals with frequencies from 0.15 to 230 MHz. The maximum rf magnetic field strength is expected to be ~ 15 G at 1 MHz with this amplifier. The amplifier can be remotely controlled and monitored through a serial port with a device server and LAN connection. A program, rfamp.tcl, written in Tcl script is used to control the device. The gain of the amplifier is variable between 33 and 58 dB. A cooling fan system protects the amplifier from overheating. When there is a significant signal reflection from the load, the gain is reduced to protect the amplifier from any damage. Such a response appears as dips in the LCR response curve as shown in figure 3.4 indicating the limit of the amplification. Some technical details of the amplifier are given in table 3.2.

Table 3.2: Technical details of the RF amplifier.

Power output (nominal) (W)	250
Power output (max.) (W)	300
Max. power gain (dB)	58
Frequency range (MHz)	0.15 - 230
Impedance (Ω)	50
Max. input (mVpp)	600

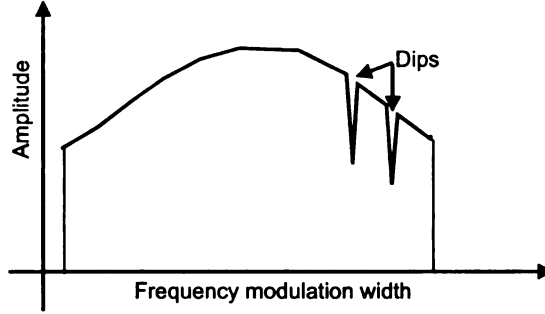


Figure 3.4: Schematic representation of dips in the LCR resonance curve because of gain reduction feature of the rf amplifier.

3.3 LCR circuitry

An efficient β -NQR technique needs relatively high rf magnetic field. To achieve high field, an LCR circuit is employed. The present LCR circuit contains an inductance (rf coil) L , a capacitance (variable capacitors) C and a resistance (50Ω) R as shown in figure 3.5. In a series LCR system, at the LCR resonance frequency, the impedance Z is equal to the resistance R of the circuit that is the minimum impedance for the circuit that could be achieved. This is caused by the equality of the inductive reactance X_L and the capacitive reactance X_C at the resonance,

$$\begin{aligned}
 Z^2 &= R^2 + (X_L - X_C)^2 \\
 X_L &= 2\pi fL \\
 X_C &= \frac{1}{2\pi fC}.
 \end{aligned} \tag{3.1}$$

Table 3.3: Technical details of the vacuum variable capacitors.

Model number	CVDD-1000-15S	C/UCSXF 1500	CMV1-4000-0005
Type	ceramic	glass	ceramic
Number of capacitors	2	2	2
Capacity range (pF)	25 - 1000	20 - 1500	25 - 4000
Max. voltage peak (kV)	9.0	4.5	5.0
Turn number	24	30	12

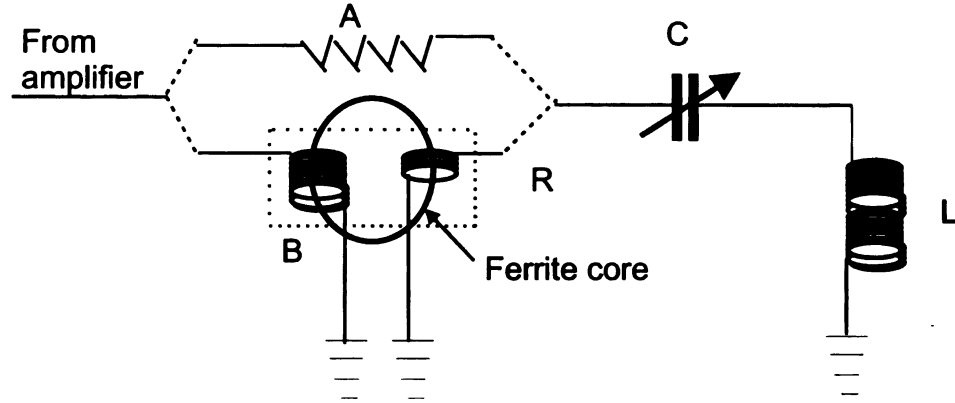


Figure 3.5: Schematic representation of the LCR circuit, where A represents 50Ω impedance matching resistor and B is the impedance matching transformer. Path A or B will be selected depending on the experimental conditions.

When X_L is equal to X_C , the impedance of the system becomes R and the frequency that gives this condition is called the resonance frequency given by,

$$f_R = \frac{1}{2\pi\sqrt{LC}}. \quad (3.2)$$

By changing L and/or C the resonance frequency varies. The C is varied using variable capacitors to tune the system for a specific frequency. There are six vacuum variable capacitors, manufactured by Jennings Technology, and their technical details are presented in table 3.3. The capacitors are remotely tuned by stepper motors, which are explained in section 3.5. Impedance of the LCR circuit should be matched to the output impedance of the amplifier, which is 50Ω . The impedance matching minimizes a reflection of the rf signal back to the amplifier from the LCR circuit that distorts the rf signal. There are two options in the system to match the impedance. One is to use

a 50 Ω , 250 W resistor and the other is to use an impedance matching transformer. The transformer has two coils around a ferrite core: the primary coil is connected to the rf amplifier and the secondary coil is connected to rf coil. Impedance matching of the transformer is achieved using the relation,

$$\frac{R_P}{N_P^2} = \frac{R_S}{N_S^2}, \quad (3.3)$$

where the R_P and R_S are the resistances and N_P and N_S are the turn numbers of primary and secondary coils, respectively. Nominal resistance of the secondary coil is $\sim 1 \Omega$, the turn number is $\sim N_P/N_S = 1/7$.

A Quality factor Q , which is given by,

$$Q = \frac{2\pi f L}{R} = \frac{f}{\Delta f}, \quad (3.4)$$

defines the resonance response of the LCR circuit. The Q is lower for the resistor system because the R is equal to 50 Ω compared with $R \sim 1 \Omega$ of transformer system. As a result, the 50 Ω resistor gives a low magnetic field strength but a broad power output distribution over a wider frequency range; most useful in the depolarization technique. On the other hand, the Q is higher for the transformer system in a narrower frequency range that is useful in the AFP technique.

3.4 Rf coil

A new coil bobbin was designed to hold thicker magnet wires and to ensure the accuracy of the angle of the implantation crystal with respect to the external magnetic field axis. The crystal holder is an integral part of the coil bobbin, and holds the crystal at an angle of 45° relative to the magnetic field. This angle minimizes scattering and self-absorption of β rays detected by up (0°) and down (180°) β detectors relative to the magnetic field. The angle between the external magnetic field and the crystal is

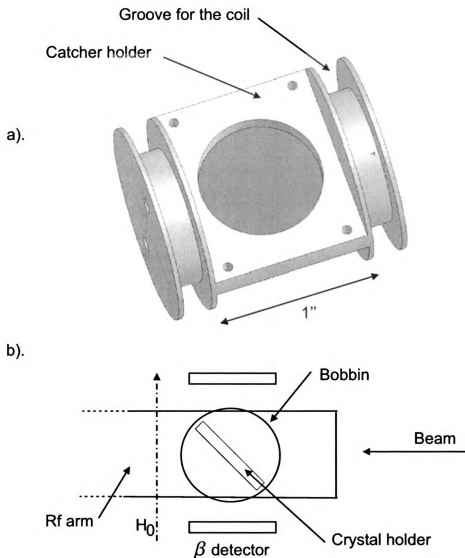


Figure 3.6: a). 3D drawing of the rf coil bobbin. b). Schematic presentation of the orientation of the coil bobbin. Catcher holder is an integral part of the bobbin and holds the crystal with an angle of 45° with respect to the H_0 .

0° . There is minimum angular dependence of rf transition frequency as a function of this angle. A schematic representation of the coil bobbin is given in figure 3.6. Several rf coils were made with the same bobbin shape and different turn numbers. Each rf coil has two equal windings in a Helmholtz-like geometry to achieve a uniform rf magnetic field in the location of the host crystal. All rf coils were wound using gauge 24, Belden magnet wire (8078). A thicker wire was required to decrease the heat generation as the high voltage drop across the coil. The inductances of the coils were

Table 3.4: Variation of inductance with turn number of rf coils.

Turn number	Inductance (μH)
15/15	14.6
17/17	20.7
20/20	27.2
25/25	44.0

Table 3.5: Variation of magnetic field strength of the rf coil (17/17) with current.

DC (A)	magnetic field strength (G)
0.0	0.0
0.1	0.3
0.2	0.7
0.3	1.0
0.4	1.4
0.5	1.7
0.6	2.0
0.7	2.4
0.8	2.7
0.9	3.1
1.0	3.5

measured with an LCR meter (ELECTRO SCIENCE INDUSTRIES - model 253) as summarized in table 3.4. The inductances were plotted as a function of turn number to establish a relationship between these two parameters as shown in figure 3.7. A variable DC power supply and a Gauss meter (FW BELL - model 5080) were used to measure the DC character of the coil using a setup as shown in figure 3.8. Results are summarized in table 3.5 and shown in figure 3.9. According to the results of this test, a relationship between magnetic field strength H_1 and current I was established as given in equation,

$$H_1 = 3.43I. \quad (3.5)$$

This relation was used to calculate the rf magnetic field strength that assuming linear relationship is valid at higher magnetic fields also, as explained in the section 4.4.

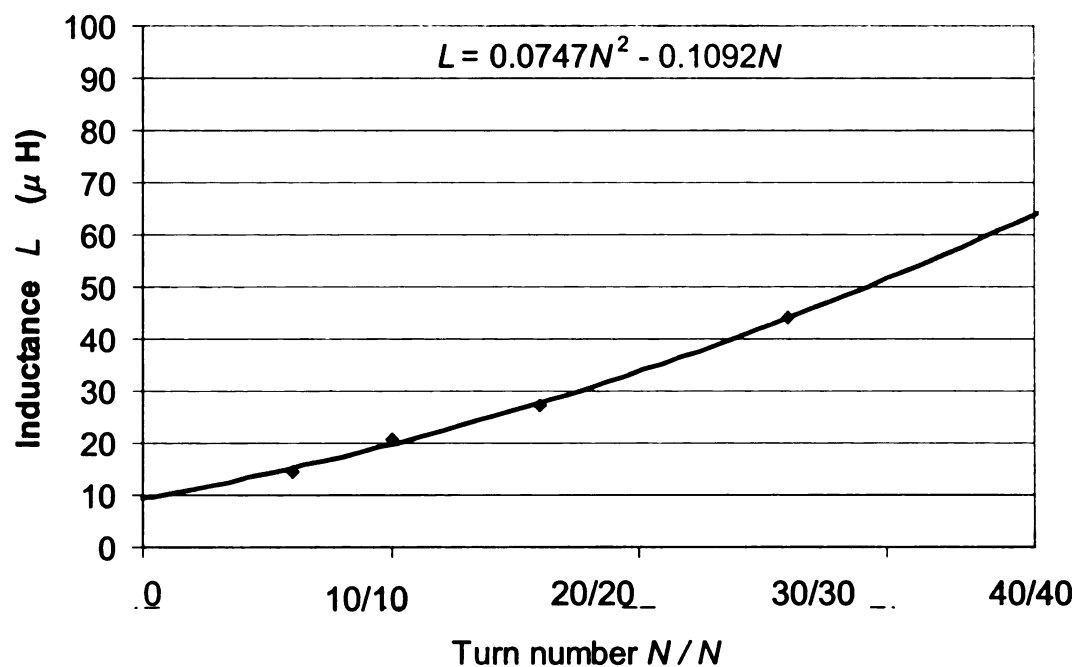


Figure 3.7: Inductance of rf coil vs turn number.

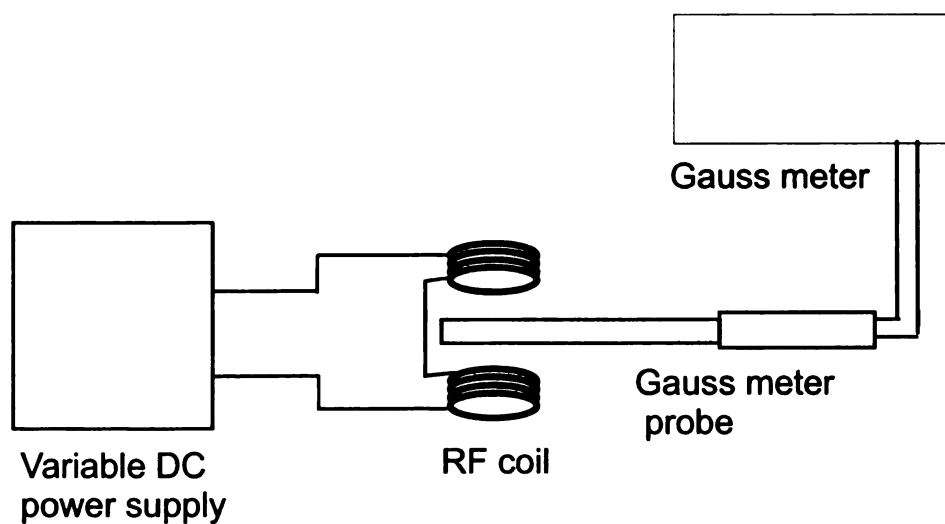


Figure 3.8: Schematic representation of the circuit used to measure the DC character of the rf coil.

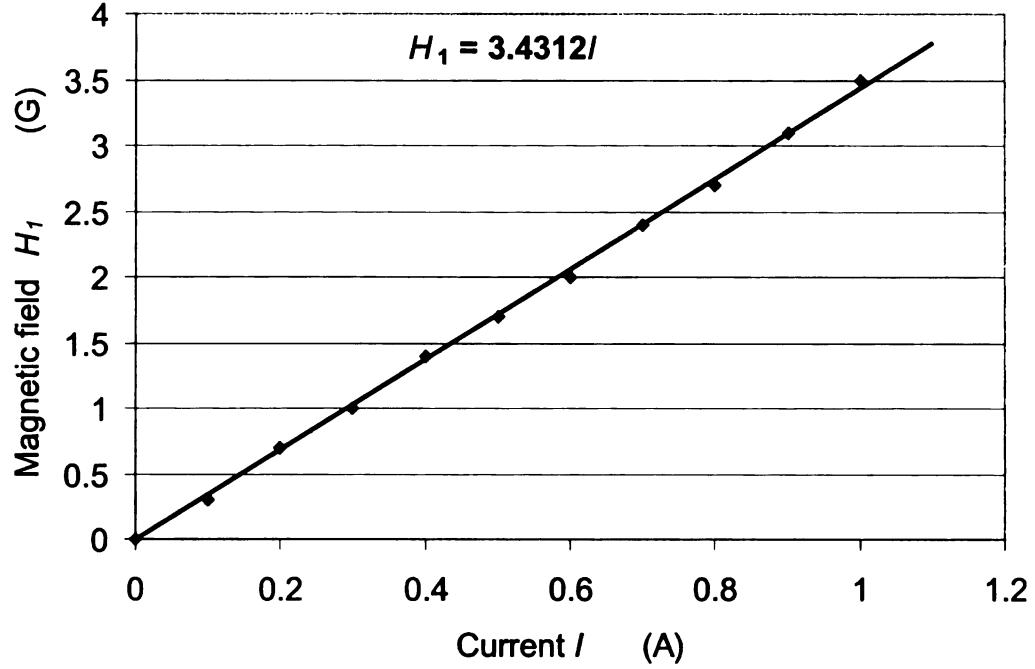


Figure 3.9: Magnetic field strength of the 17/17 coil as a function of direct current.

Table 3.6: Node address hardware configuration.

	Node addresses															
J3	1	2	3	4	5	6	7	8	9	10	11	12	13	14	15	16
1		X		X		X		X		X		X		X		X
2			X	X			X	X			X	X			X	X
3					X	X	X	X					X	X	X	X
4									X	X	X	X	X	X	X	X

3.5 Stepper motor controlling system

In experiments to search a nuclear quadrupole resonance by scanning the rf, different of rf signals have to be applied. For each signal, the capacitors require adjustment to have correct impedance matching. The variable capacitors are remotely adjusted by stepper motors, which are driven by motor controllers with serial port connected to a device server and LAN. The program testR4.tcl is a Tcl script written to control the stepper motors. The motor controllers are manufactured by Eggert Electronics, model

Table 3.7: Specifications of relay switches. Switch on and off times were experimentally measured.

Type	GR6CBA 335	GR6HBA 318	GH 1
Voltage (kV _{peak})	2	7	2.5
Max. DC current (A)	6	10	25
On time	200 μ s	1.6 ms	3 ms
Off time	160 μ s	0.8 ms	1.2 ms
Coil resistance (Ω)	1000	1000	80
Coil voltage (V)	24 -30	24 - 31	12

SSC1B, and six controllers are connected in a "daisy chain" as shown in figure 3.10 to control the six stepper motors manufactured by Superior Electrics, model M061. In the daisy chain, control signals flow through controllers in series. A node address is assigned to each motor controller by setting J3 jumpers on the controller board as shown in the table 3.6. The motor controller board can be damaged if the power is supplied without connecting a motor. To avoid any accidental damage to the motor controllers, the power is supplied to a motor controller through a relay switch, which is activated only with jumper pins in an 8-pin high-density Amp connector (TYCO ELECTRONICS- Model 206434-1) as shown in the figure 3.11. Without connecting stepper motors to the Amp connectors, the power supply for the motor controllers remains disconnected. A motor controller box designed at the NSCL contains all the motor controller-boards, the motor controller-relay switches, DC power supply and device server for LAN connection.

3.6 Vacuum relay switching

In the β -NQR technique, several rf signals are applied within a very short time interval in millisecond range. The switching time between rf signals should be very short, few milliseconds, because of the short lifetimes of the exotic nuclei of interest. The rf switches also should be able to handle high power. Therefore high power vacuum relay switches were selected. The switching times were measured for three types of

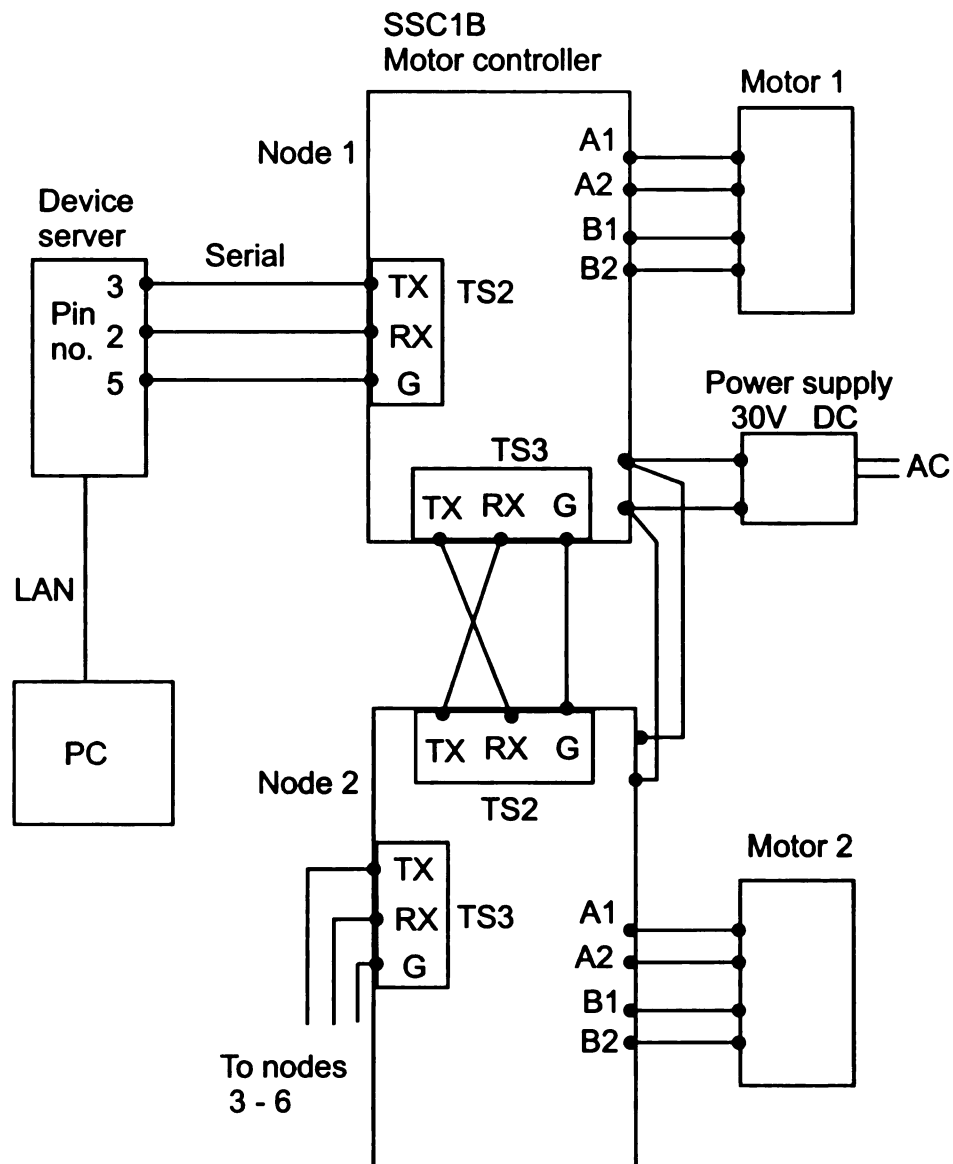


Figure 3.10: Schematic representation of stepper motor controlling system. Each controller controls one motor and 6 controllers are connected in series (daisy chain)

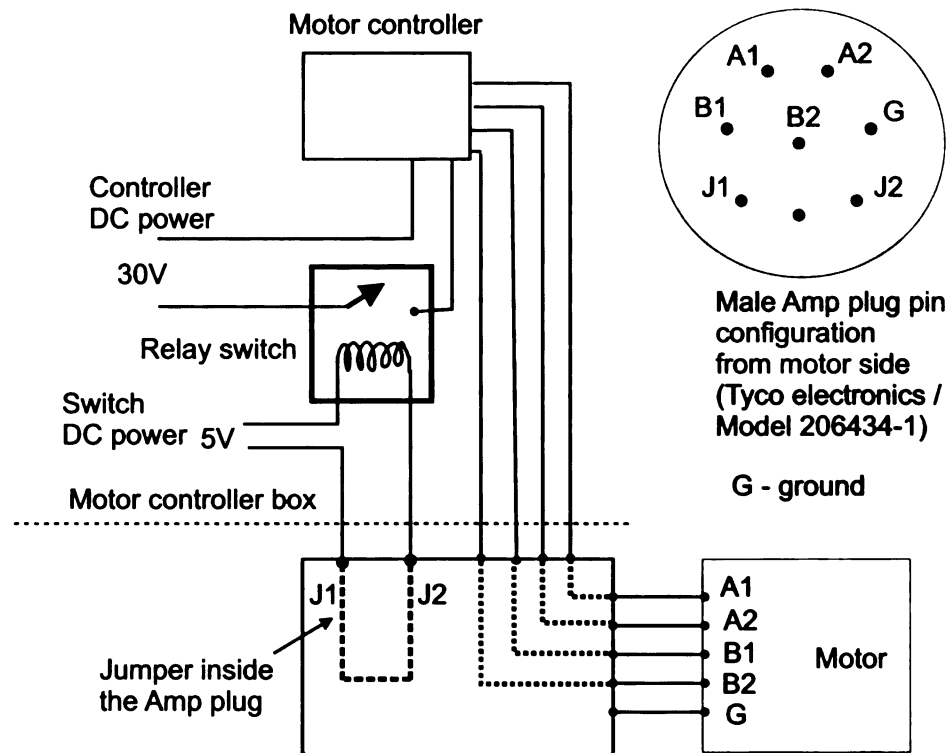


Figure 3.11: Schematic representation of power supply for motor controllers. The jumper and the relay switch make sure that the power to the controller remain turned off, when motors are not connected.

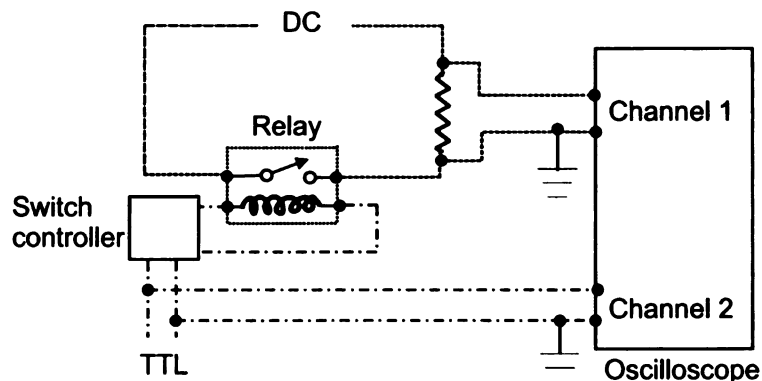


Figure 3.12: Schematic representation of switch time measuring circuit. A DC signal was switched by a TTL signal and an oscilloscope measured both signals.

Table 3.8: Switch response time of six relays (GR6HBA 318) measured after constructing the system.

Switch number	On time (ms)	Off time (ms)
1	1.5	0.6
2	1.5	0.7
3	1.4	0.7
4	1.6	0.7
5	1.7	0.8
6	1.8	0.7

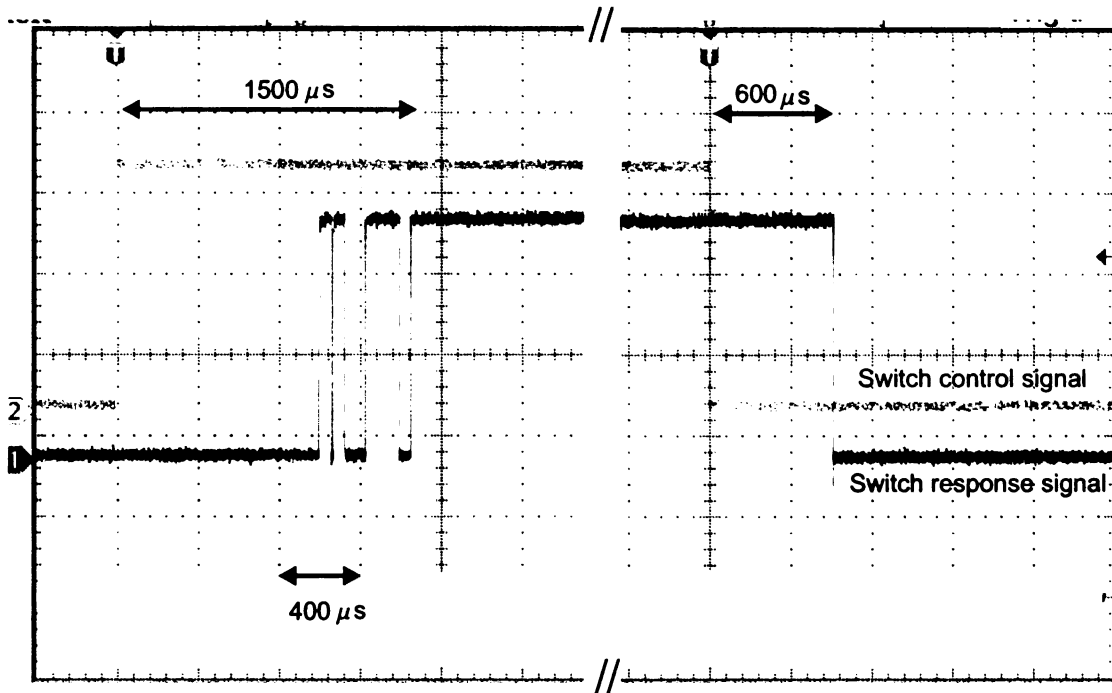


Figure 3.13: Response time of switch number 1, extracted from oscilloscope.

vacuum relay switches manufactured by GIGAVAC with different maximum voltage and current limits. Some technical details of those relay switches are given in table 3.7. To measure the switching time, a TTL signal was used as the control signal of the relay through a switch driver circuit and a DC signal was switched on and off by the relay. Both switch on time and off time were measured with an oscilloscope as shown in figure 3.12. The results are summarized in table 3.7. The switching times of all the relays are short enough for the β -NQR system. The GR6HBA318 relay

switch was selected for the system because of the high maximum voltage and current and sufficient switching time, considering the decay lifetime of the ^{37}K in the first experiments that would be done to test the system as explained in the chapter 5. However, depending on the experimental requirements, other types of relay switches could be used. Six GR6HBA318 switches were purchased and installed in the rf box and the switching times were checked for each relay. The results are summarized in table 3.8 and a typical response is shown in figure 3.13. During the switch on time period, a jitter was observed as the mechanical nature of the relays. A switch on time of 2 ms would ensure that mechanical operation of relay close is complete.

The relay switches are controlled by switch controllers, whose circuit diagram is given in figure 3.14. The RPV071 module triggers these switch controllers, which is explained in section 3.7. The relay switch controller has two main parts as shown in the figure 3.14. The left part of the equipment will be located in the Data U, including a NIM standard chassis that accepts the TTL control signals from RPV071. The right part of the equipment is located inside the rf box, which will be placed inside the vault during the experiment. The vault equipment accepts TTL signals from the Data U equipment through a patch panel and works as a signal amplifier. The two parts of the controller are separated by an optical coupler (4N35) to prevent any noise coming from high power rf signals to the data U. Coil resistance of the present relays is $1000\ \Omega$ and range of operating voltage is 24 to 30 V. The voltage across the relay coil is determined by a resistor labeled as R1 in the figure 3.14, which is $27\ \Omega$ for GR6HBA318 switches.

The vacuum relay switching is operated in cold switching mode. Therefore, rf signal is on and off before the relay switch is on and off, respectively as shown in figure 3.15. This will prevent high power sparking at the contacts of the switches and possible distortion of the rf signal. This cold switching mode will also increase the lifetime of the switches.

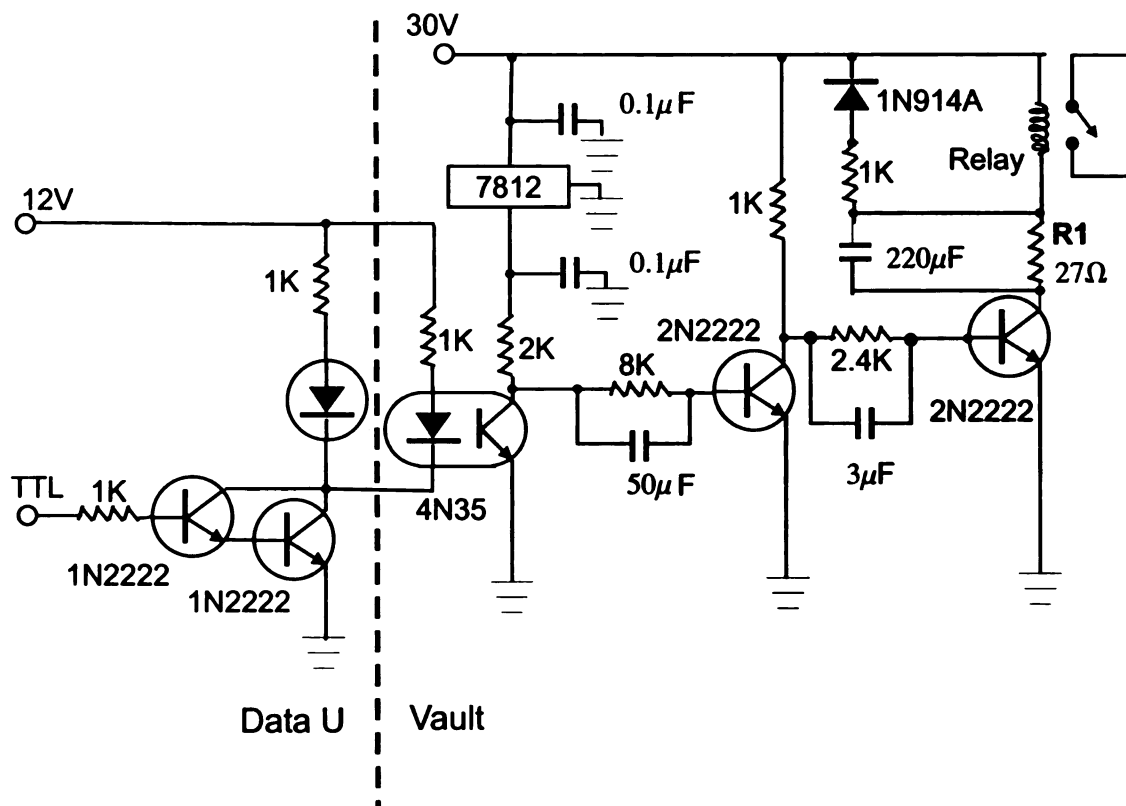


Figure 3.14: Circuit diagram of relay switch controllers. The two parts of the circuit are separated by an optical coupler (4N35) to minimize the possible noise coming to the data U from the rf box.

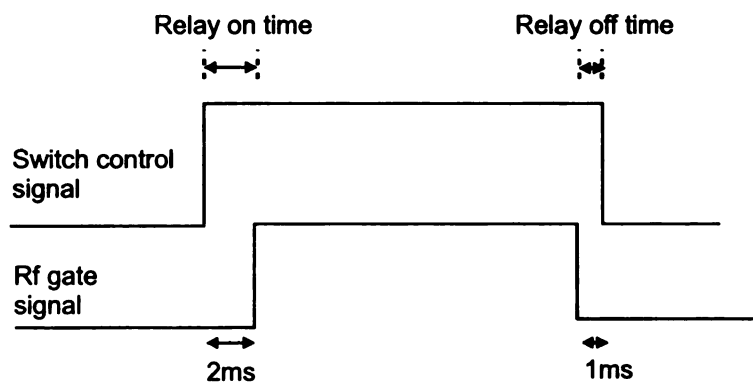


Figure 3.15: Relay switch control and rf gate signals. The rf gate signal is open within the limits of switch control signal to avoid any hot switching.

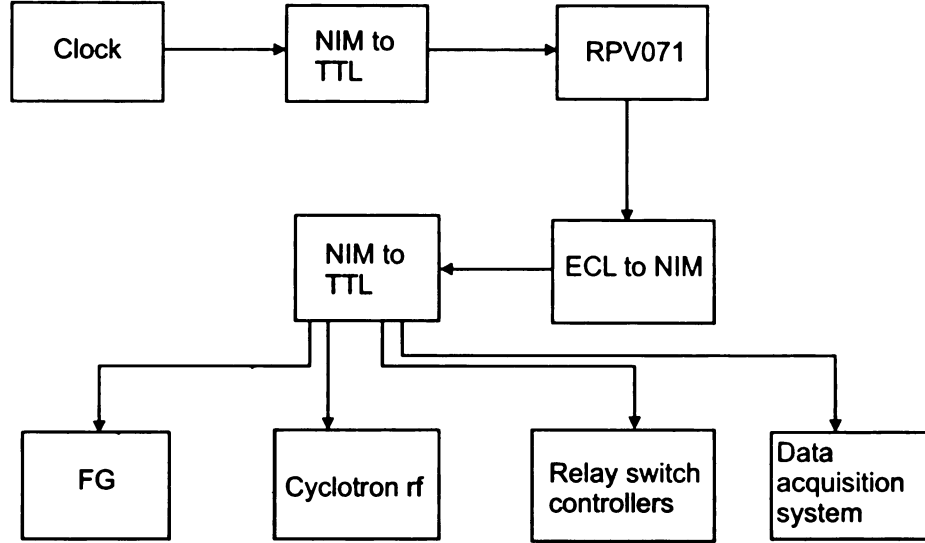


Figure 3.16: Schematic representation of triggering and timing system controlled by the RPV071.

3.7 RPV071 module

RPV071 is a 32-channel pulse pattern generator manufactured by REPIC CORPORATION according to the VME standards. The RPV071 controls all the triggering and gating signals of experimental components and timing programs as shown in figure 3.16. A timing sequence is written to the memory of the RPV071 through the VME bus. The memory of the RPV071 has 65K bins and each bin is divided into 32 channels. Writing 0 or 1 to each channel in the memory bins will result in low or high output levels respectively, according to the clock signal given to the RPV071 as shown in figure 3.17. Time resolution of the RPV071 depends on the clock signal that can either be external or internal (50 MHz) source. As an example, if the frequency of the clock signal is 2000 Hz, timing resolution is 0.5 ms (the bin position is incremented every 0.5 ms). Since the total memory length is 65K long word, the maximum time span would be about 30 s. For the proposed β -NQR experiments at the NSCL, several timing programs will be used. Figure 3.18 shows a possible timing program for the pulsed-beam depolarization method. Timing programs for continuous-beam depolarization method and AFP method are shown schematically in figure 3.19 a) and

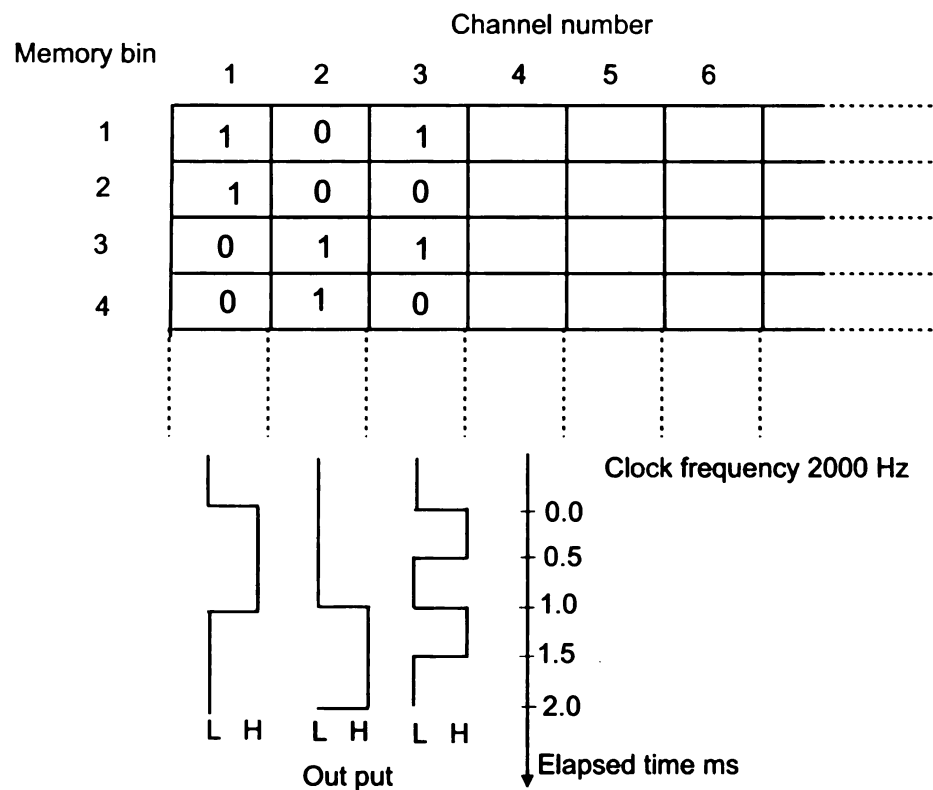


Figure 3.17: Schematic representation of writing a program to the memory of RPV071. The output signals are shown in the lower part with the external clock frequency of 2000 Hz.

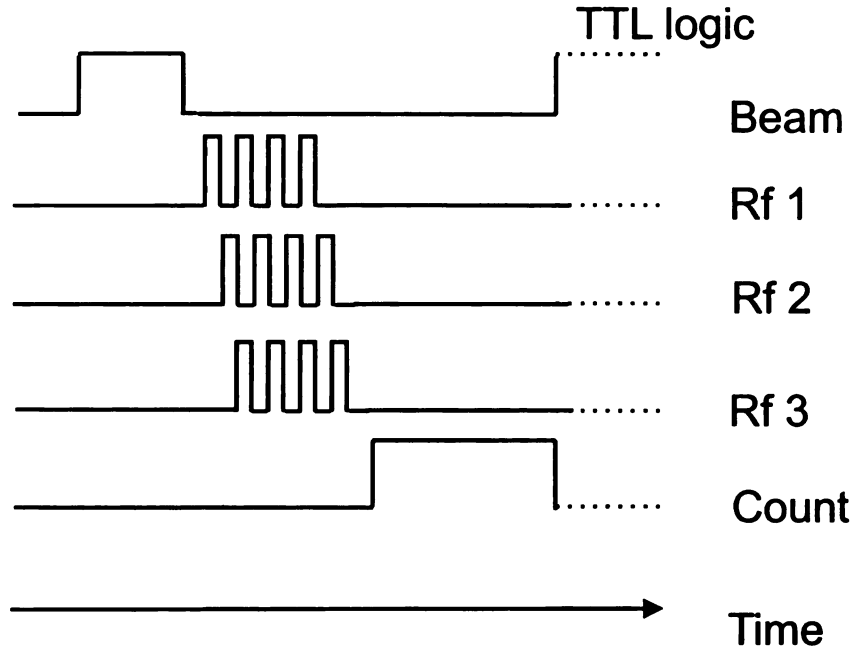


Figure 3.18: Schematic representation of one cycle of the timing program of pulsed-beam depolarization method for the $I=3/2$ nuclei. Beam is pulsed and when beam is off rf signals are applied. At the end of rf signal application, the counting gate is opened.

b), respectively. A control program for the RPV071 can manage experiments using continuous beam depolarization (NQR ONOFF), pulse beam depolarization (NQR DEP) and AFP (NQR AFP). All programs are currently capable of handling up to the $I=2$. In all three programs, rf on time, relay switch on and off times and switch configuration must be specified. For the NQR ONOFF program, the counting on and off times must be specified. The NQR DEP program requires the beam on and off times and the number of repetitions of the rf in a cycle. For the NQR AFP program, the beam time and the rf count on time are needed. New timing sequences can be programmed depending on the different experiments.

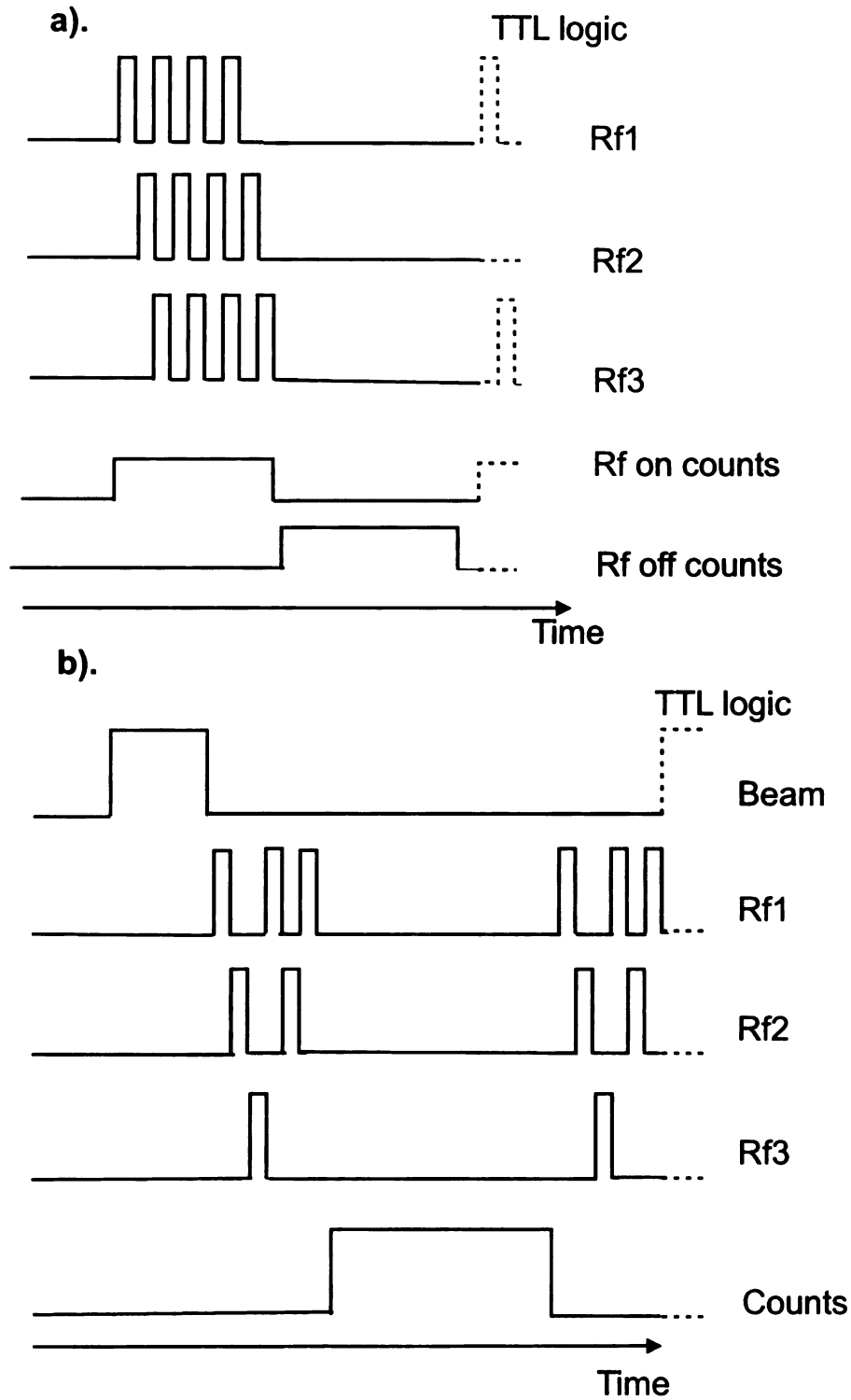


Figure 3.19: Schematic representation of one cycle of the timing programs for $I=3/2$ nuclei a). Continuous beam depolarization technique; Selecting IMM trigger (internal), several frequency sweeps occur during one rf gate signal b). AFP technique. In between two beam pulses, rf signals are applied before and after counting.

Chapter 4

β -NQR system tests

Several tests were performed to evaluate individual components and the whole β -NQR system.

4.1 Calibrating of stepper motor controllers for variable capacitor operation

For the safety of the motor controlling system, upper and lower limits for the capacitors were set in the motor controlling program. A LCR meter was used to identify the lowest and highest capacitance of each capacitor. Thereafter, the number of steps taken by a stepper motor required to cover this range of capacitance was determined. The turn number of a capacitor was calculated using the number of steps taken by a stepper motor per revolution (200 steps/revolution). The results are summarized in table 4.1.

Table 4.1: Upper and lower limits for variable capacitors. The number of motor steps needs to cover the capacitance range of each capacitor was measured and lower and upper limits were set in the motor controlling program.

Capacitor /Motor number	Lower position (steps)	Capacitance μF	Upper position (steps)	Capacitance μF	Turn no.
01	0	25.2	2400	4000	12
02	0	24.7	2400	4000	12
03	0	28.9	6500	1500	32.5
04	0	34.7	5900	1500	29.5
05	0	41.7	4900	1000	24.5
06	0	39.5	4950	1000	24.75

4.2 Testing the whole system

4.2.1 RF leakage test

An rf leakage test was performed to make sure that system works without radiating significant rf levels to the surroundings. An electro-magnetic radiation monitor (NAR-DAR / 8616) was used and no significant leakage of rf field was observed (less than 0.1 mW/cm^2) around the well-shielded rf box. The rf coil was placed inside the vacuum chamber, which has several openings. Significant rf field was observed, about 100 mW/cm^2 , near these openings. During an experiment all these openings are closed, except the plastic windows which facilitate the β ray emission to the detectors. The rf leakage near the window was measured as a function of the distance and summarized in table 4.2. However, when the distance is around 6 inches, the measured rf field is negligible. This window will be inside the NMR magnet during normal operations. During the bench-top tests, all the vacuum chamber openings have to be covered with aluminum foil that minimize the rf leakage.

4.2.2 Cold switching confirmation

Before applying high power to the system, each variable capacitor was tested by supplying $2000 \pm 100 \text{ kHz}$ rf with 100 ms sweep time without amplification. Switch

Table 4.2: Results of the rf leakage test. The rf leakage was measured near the window of the vacuum chamber, where rf coil is placed during an experiment.

Distance from window of the vacuum chamber	Rf strength (mW / cm^2)
0	104
1	12.5
2	7.0
3	1.2
4	0.7
6	0.05

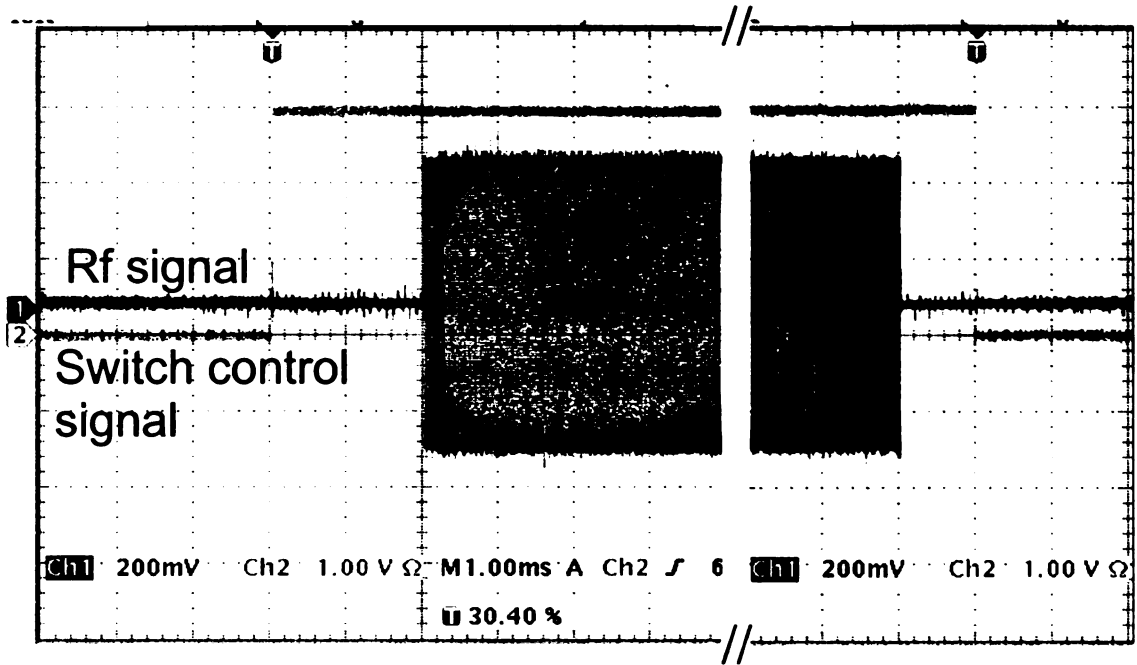


Figure 4.1: Switch control signal and rf signal from switch one and capacitor one extracted from oscilloscope.

on time and off time were set to 2 ms and 1 ms, respectively for all switches. The output voltages of the function generators were set to 500 mVpp and the switch on and off times were measured. One of the main objectives of this test is to make sure that system is working in the cold switching mode. According to the results, the time differences between switch on and rf on, and switch off and rf off were in safe time limits specified by the switch control program as shown in figure 4.1.

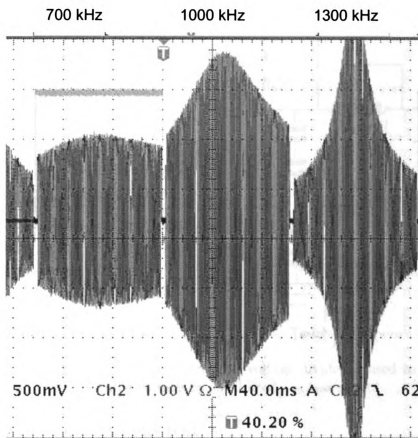


Figure 4.2: LCR resonance frequencies at low power.

4.2.3 Low power test

The whole system was tested with three different frequencies at low power, for which three LCR circuits with capacitor numbers 1, 2 and 3 were used. Rf signals with frequencies 700 ± 100 kHz, 1000 ± 100 kHz, 1300 ± 100 kHz were applied to the capacitors 1, 2, and 3, respectively. The NQR ONOFF timing program was used with a 500 ms on time and a 500 ms off time. Sweep time was set to 100 ms. The output voltages of the function generators were 500 mVpp. Three capacitors were tuned, using motor controller program to have the resonance frequencies as shown in the figure 4.2.

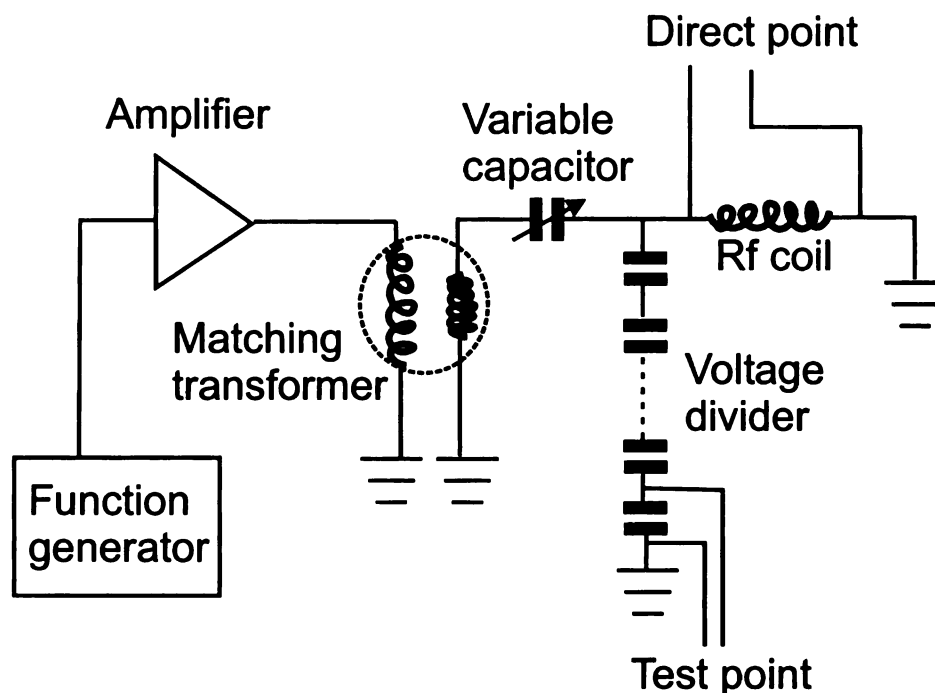


Figure 4.3: The circuit for the power tests. A voltage divider is used to reduce the high voltages to a measurable voltage by oscilloscope at test point.

4.2.4 Maximum rf field test

In order to demonstrate a capability of the system to perform, for example, quadrupole moment measurement of ^{37}K that is explained in chapter 5, the whole system was tested with three transition frequencies. The 250 W rf amplifier was used with gain of 58 dB. The NQR ONOFF timing program was used with a 5000 ms on time and a 5000 ms off time. Sweep time was set to 100 ms. At first, at low input region (10 and 20 mVpp) output voltages were measured directly (direct point) and through a voltage divider (test point) to find the ratio between these values. A capacitor bridge was used as a voltage divider. A simplified version of this circuit is shown in figure 4.3.

The input voltage was increased gradually and the output voltage was measured at the test point. The direct output was calculated using the ratio established between direct and test point voltages. The results are shown in table 4.3. Beyond the input of 220 mVpp, interference of rf signal was observed due to the rf reflection. Measurements

Table 4.3: High power test of the whole system. Values given in brackets are not directly measured.

Capacitor	Frequency kHz	Input (mVpp)	Output direct (Vpp)	Output test point(Vpp)	Ratio	H_1 (G)
1	700±10	10	92	3.9	23.4	1.8
		20	150	7.8	23	1.9
		120	(1049)	45.6		10.9
		200	(1619)	70.4		16.9
		220	(1748)	76.0		18.2
2	1200±10	10	157	6.6	23.6	0.9
		20	313	13.6	23	1.9
		120	(2760)	78.4		10.9
		200	(2714)	118		16.5
		220	(2898)	126		17.6

were stopped at 220 mVpp due to the distorted response curve. The rf magnetic field was calculated using the equation,

$$H_1 = m \frac{V_{pp}}{2\pi f L} \frac{1}{4}, \quad m = 3.43I, \quad (4.1)$$

where m is established between magnetic field strength and the current in the DC character measurement of the rf coil and V_{pp} is the voltage across the rf coil. Maximum magnetic field strengths were calculated for ^{37}K experiment, are at 700 kHz and 1200 kHz to be 18.2 G and 17.6 G, respectively. These field strengths are sufficient to conduct AFP experiments on ^{37}K and ^{35}K .

4.2.5 Capacitance limits on LCR circuit

When all the motor positions are set to zero, the system shows resonance at about 2100 kHz indicating minimum capacitance of the system of ~ 270 pF. At maximum capacitance of the 4000 pF capacitor, the lowest resonance frequency is ~ 400 kHz. Combining the two 4000 pF capacitors reduces the maximum resonance frequency to ~ 370 kHz.

Chapter 5

β -NQR Application to $^{35,37}\text{K}$

The new β -NQR system is capable of measuring quadrupole moments of nuclei up to $I=2$, according to the results of system tests explained in the last chapter. In this chapter, the proposed experiments to measure quadrupole moments of the sd shell nuclei ^{37}K ($I^\pi=3/2^+$, $t_{1/2}=1.22$ s) and ^{35}K ($I^\pi=3/2^+$, $t_{1/2}=178$ ms) are discussed.

5.1 Quadrupole moments of the nuclei in sd shell

A good agreement between experimental [2] and theoretical [13] (OXBASH) quadrupole moments for isospin $T=1/2$, sd shell nuclei, in general, is observed as shown in figure 5.1. The trend of the quadrupole moments can be explained as follows. When one single nucleon is in the $1d_{5/2}$ shell, the quadrupole moment takes a negative value. The quadrupole moment changes sign as the $1d_{5/2}$ shell is filled, in agreement with the single particle shell model. When the valence nucleons occupy the $2s_{1/2}$ orbit, the quadrupole moment is zero, as the total angular momentum is equal to $1/2$. When the $1d_{3/2}$ shell has one nucleon, the quadrupole moment again is negative and changes sign as the $1d_{3/2}$ shell is filled. The same type of systematic behavior of the quadrupole moment is expected for $T=3/2$ nuclei in the sd shell. However, as

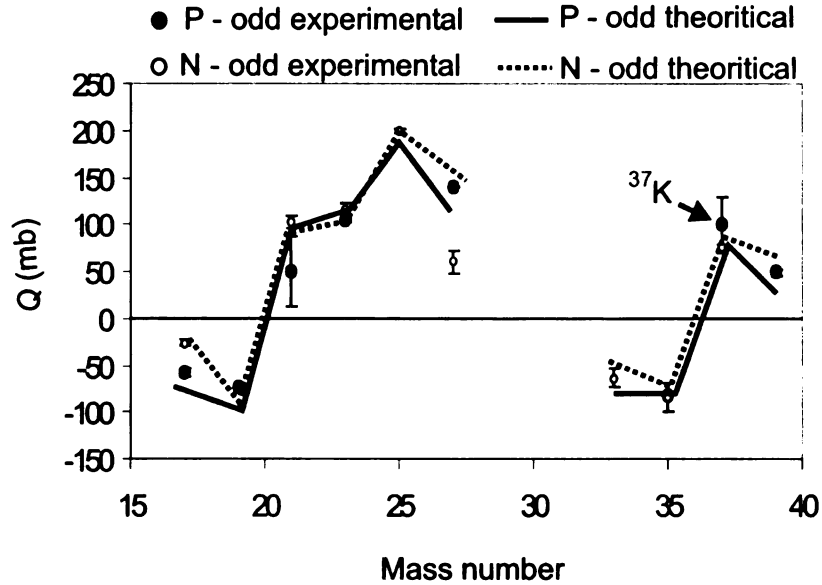


Figure 5.1: Experimentally measured quadrupole moments of $T=1/2$ nuclei in the sd shell, which have good agreement with theoretical prediction (OXBASH).

few (about 7 nuclei) measured quadrupole moments are available for $T = 3/2$ nuclei, especially in the neutron-deficient region. Measuring the quadrupole moments of the $T = 3/2$ nuclei is essential to test the predictions of standard shell model and other mean-field theories far from the stability line.

5.2 Quadrupole moments of potassium isotopes

Only four nuclear quadrupole moments have been measured for potassium isotopes as shown in figure 5.2. ^{39}K and ^{41}K are stable isotopes and ^{40}K is a long-lived isotope at the line of stability. ^{37}K is the only unstable potassium isotope that has a known quadrupole moment lying in the neutron-deficient region. The odd- A K isotopes are believed to have one proton hole in the $1d_{3/2}$ shell. The quadrupole moment should be positive according to the single-particle shell model. When the K isotopes become more neutron-deficient, a significant deviation from shell model-expectations may occur, because of the low proton binding and core deformation.

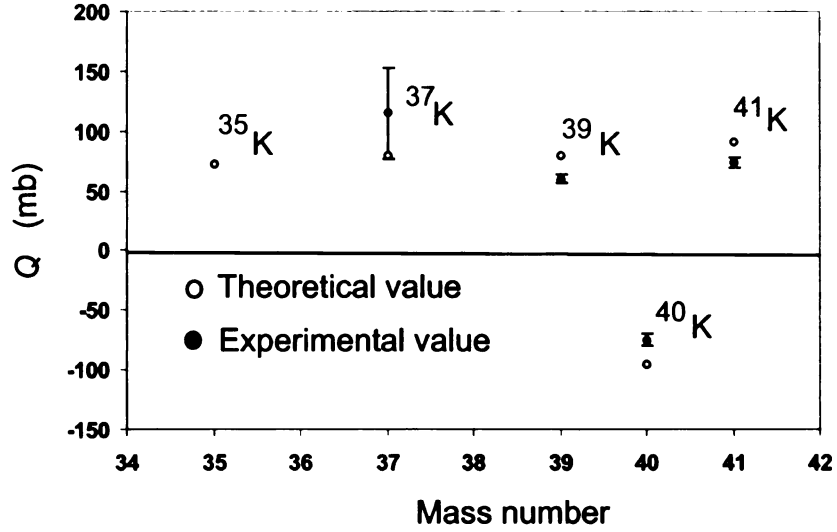


Figure 5.2: Measured quadrupole moments of potassium isotopes of ^{37}K [15], ^{39}K [16], ^{40}K [17] and ^{41}K [18] and theoretical prediction (OXBASH)(model space sd and interaction w).

Already, ^{37}K exhibits a large quadrupole moment than, ^{39}K and ^{41}K , although the experimental value has a large error. Therefore, high precision measurements of the quadrupole moments of the neutron deficient K isotopes are of great interest. T. Minamisono *et al.* measured quadrupole moment of ^8B as 68.3 ± 2.1 mb [6] and it is twice as large as shell model prediction. The proton separation energy of ^{35}K is 78 keV and much lower than that of ^8B (137.5 keV), therefore it is expected that the proton distribution spreads out radially and give rise to a higher quadrupole moment than predicted. If quadrupole moment of ^{35}K is higher than predictions indicates the presence of unusual core deformation. T. Minamisono *et al.* claimed that ^8B is a proton halo nuclei. The low separation energy of ^{35}K makes it a candidate for a proton halo as well.

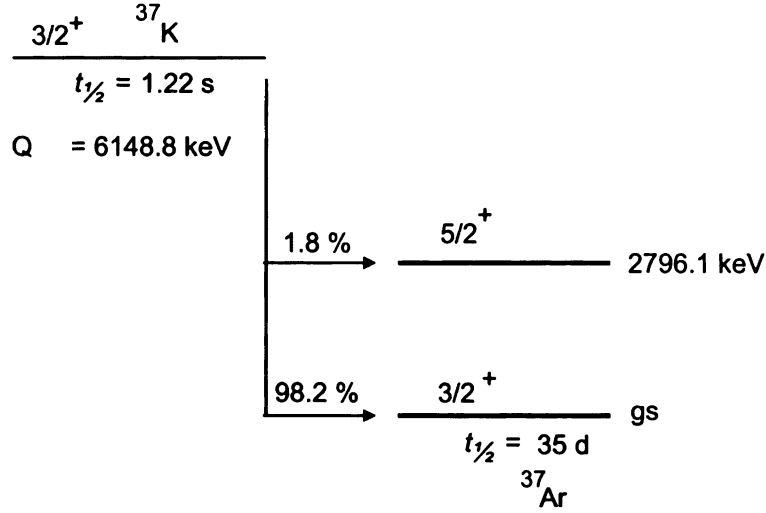


Figure 5.3: Partial decay scheme of ${}^{37}\text{K}$. The energy levels are not in scale.

5.3 Quadrupole moment measurement of ${}^{37}\text{K}$

${}^{37}\text{K}$ is a β^+ emitter with a half-life of 1.22 s. ${}^{37}\text{K}$ decays predominantly to the ground state of ${}^{37}\text{Ar}$ with a branching ratio of 98.2% as shown in the figure 5.3. This main β decay branch is of a Gamow-Teller and Fermi mixed type with the asymmetry parameter of -0.598 [19], [20]. The quadrupole moment of ${}^{37}\text{K}$ was measured as $100 \pm 30 \text{ mb}$ [15] by the laser-spectroscopic technique on an atomic beam. The quadrupole moment of ${}^{37}\text{K}$ will be re-measured for commissioning of the new β -NQR system, since its value is roughly known and large polarization of ${}^{37}\text{K}$ has been established [11]. A potassium di-hydrogen phosphate (KH_2PO_4) or KDP single crystal will be used as the host crystal because its electric field gradient, q , at the potassium site is experimentally known [21]. The asymmetry parameter of the electric field gradient η , is equal to zero because of its symmetric crystal structure (tetrahedral) [22], which gives a simple resonance structure. The nuclear energy levels can be calculated using the first order perturbation theory to obtain the transition frequencies. From the quadrupole moment of ${}^{37}\text{K}$ and q in KDP, the quadrupole coupling constant, eqQ/h , for ${}^{37}\text{K}$ is $3.4 \pm 1 \text{ MHz}$. The corresponding set of three transition frequencies for the $I=3/2$ ground state are 413 kHz, 1286 kHz and 2113 kHz at the magnetic field

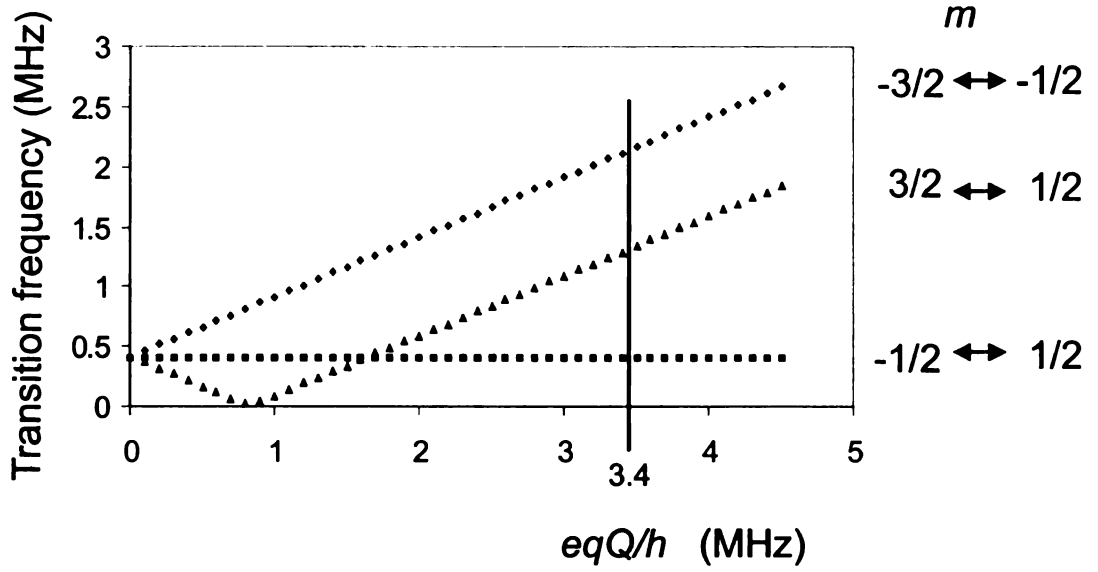


Figure 5.4: Transition frequencies for the quadrupole moment (^{37}K) calculated from first order perturbation theory at 0.4 T. The dots are the calculated transition frequencies and the solid line represents three transition frequencies corresponding to the known coupling constant for ^{37}K implanted into KDP.

strength of 0.4 T as shown in figure 5.4. The set of three frequencies will be scanned in accordance with the calculation shown in figure 5.4 to cover the error associated with eqQ/h . The quadrupole moment of ^{39}K will be used as the reference to deduce the quadrupole moment of ^{37}K . According to the literature, the quadrupole moment of ^{39}K is 61.5 ± 1.5 [23]. There for the systematic error, that can be expected for the quadrupole moment of ^{37}K will be less than 5%. The statistical error will be very small because of the high counting ratio of ^{37}K and approximately 30 hrs counting time may be enough to achieve this statistics.

5.4 Quadrupole moment measurement of ^{35}K

^{35}K is a β^+ emitter with a half-life of 178 ms. The ^{35}K decay has four dominant transitions including transitions to three different excited states and to the ground state of ^{35}Ar as shown in figure 5.5. The asymmetry parameter is uncertain (estimated range: $+0.60 - -0.32$) but spin polarization was observed in a previous NSCL experiment

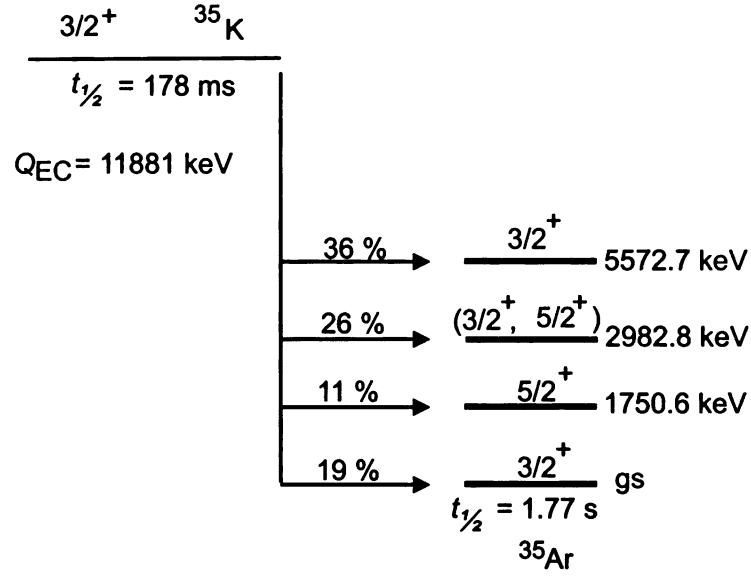


Figure 5.5: Partial decay scheme of ${}^{35}\text{K}$. The energy levels are not in scale.

(01039-II) [24]. The quadrupole-coupling constant for ${}^{35}\text{K}$ is $2.3 \pm 0.7 \text{ MHz}$, based on the known q in KDP and the theoretically-calculated (OXBASH) quadrupole moment of 72 mb. Therefore, the set of three transition frequencies are 553.43 kHz, 594.56 kHz and 1744.56 kHz at 0.3 T as shown in figure 5.6. Assuming 30% error in the coupling constant, the set of 3 frequencies will be scanned in accordance with the calculation in figure 5.6.

5.5 Experimental details

The production yield and the polarization of ${}^{37}\text{K}$ and ${}^{35}\text{K}$ were measured via intermediate-energy pick up reactions in the previous NSCL experiments (01039 -I and II) [11], [24]. For the production of ${}^{37}\text{K}$, the collision between the primary beam of ${}^{36}\text{Ar}$ with an energy of 150 MeV/nucleon and a 564 mg/cm^2 ${}^9\text{Be}$ target will produce ${}^{37}\text{K}$ through the charge pickup reaction. The beam will be set at an angle of $+2^\circ$ relative to the normal beam axis to produce a spin-polarized beam. The full angular acceptance of the A1900 will be used and the momentum acceptance limited to 1% using a slit at the second intermediate image. A momentum $+0.5\%$ higher than the peak yield

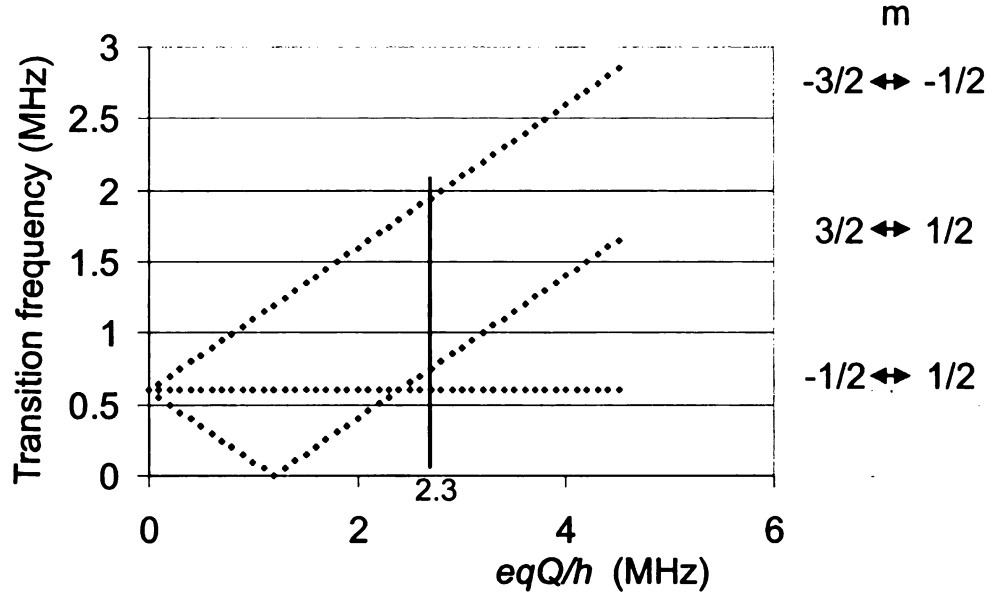


Figure 5.6: Transition frequencies of ^{35}K calculated by first order perturbation theory at 0.3 T. Dots are calculated transition frequencies and solid line represents three transition frequencies that correspond to the coupling constant.

momentum of ^{37}K will be chosen. An achromatic wedge (450 mg/cm^2 , Al) will be used at the intermediate image to separate secondary particles based on the relative energy loss. Under an external magnetic field, ^{37}K will be implanted into the host KDP crystal, as shown in figure 5.7, tilted by 45° relative to the secondary beam axis to increase the effective implantation thickness and to minimize the absorption and scattering of β rays from stopped nuclei by the crystal itself. According to the previous ^{37}K experiment (01039-I) at the NSCL, the ^{37}K beam will have high purity (98%, [11]). Particle identification will be performed using a PIN detector in the beam line just upstream of the NMR magnet by ΔE -TOF (between PIN and rf of the cyclotron) method. The final counting rate of β particles in two sets of detectors is predicted to be 350 pps/pnA (based on 50 pnA of primary beam intensity).

^{35}K nuclei will be produced in the same charge pickup reaction as ^{37}K but followed by two-neutron evaporation. The ^{35}K beam will be treated in the same way as the

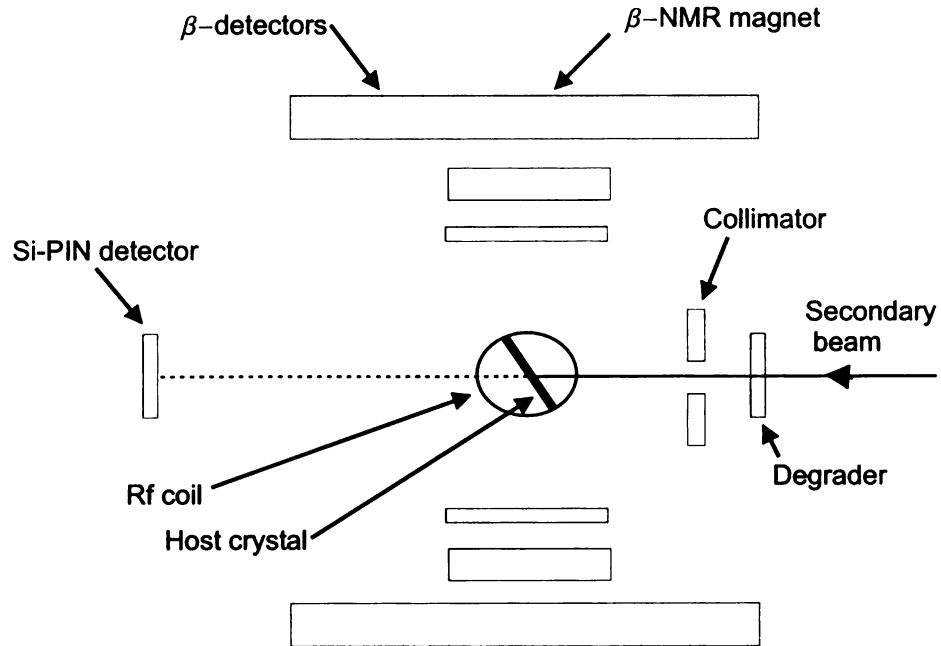


Figure 5.7: β -NMR setup at NSCL.

^{37}K beam . The final counting rate of β particles in two sets of detectors is predicted to be 5 pps/pnA based on the previous ^{35}K experiment (01039-II) at the NSCL. ^{34}Ar constitutes a significant contaminant in the ^{35}K beam. A shield to cut off β rays with energy lower than about 5000 keV, will be used to reduce the ^{34}Ar contribution to the spectrum.

Chapter 6

Summary

The Quadrupole moment is a direct measure of the deviation of charge distribution of a nucleus from its spherical shape. Therefore, it is zero for spherical-shaped nuclei and takes positive value and negative value for prolate-shaped and oblate-shaped deformed nuclei, respectively.

The quadrupole moment is used as an important observable to investigate the nuclear structure, as it changes sign over a shell indicating the presence of a proton hole or an odd valence proton, respectively. The quadrupole moment can be used as evidence for the presence of configuration mixing in the nucleus. Core deformation is also a concept that can be investigated by quadrupole moment measurements, especially in the heavy-mass nuclei. The measured large quadrupole moments of heavy nuclei helped to establish the collective effects of valence nucleons on the core deformation. The quadrupole moment can be used to extract the charge radius of the nucleus, which is important to understand the radial extent of a nucleus.

There are several techniques to measure the quadrupole moments including laser spectroscopy, low temperature nuclear orientation, nuclear quadrupole resonance technique, and microwave spectroscopy. Each technique has its own advantages and disadvantages.

The β -NQR technique moreover, is probably the most effective method to mea-

sure nuclear electric quadrupole moments of exotic nuclei. The technique requires an ensemble of spin-polarized β emitting nuclei. At the NSCL, nuclear spin polarization is produced directly in intermediate-energy heavy-ion reactions. Both nucleon pickup and removal reactions can be used to generate polarizations of order 1% or greater for nuclei a few nucleons away from the projectile.

The β -NQR method requires a host material with a non-cubic lattice structure. Polarized nuclei are implanted in a crystal with an electric field gradient placed in a strong magnetic field. The strong magnetic field helps to preserve the spin polarization that can be depolarized due to the spin-lattice relaxation and spin-spin relaxation processes. In addition, Zeeman splitting is induced by the magnetic field. The electric interactions shift the evenly spaced energy levels because of the electric field gradient of the host crystal. The spin manipulation is performed by applying rf magnetic field perpendicular to the external magnetic field. Several different transition frequencies are required for the depolarization because of the uneven energy gaps among magnetic sub-states. There are two spin manipulation techniques as depolarization and AFP technique. In the depolarization technique, spin precesses around the effective magnetic field that is a result of the external magnetic field and at the resonance, the spin precess around the rf magnetic field and the spin polarization vanishes. In the AFP technique, an rf is swept once over the resonance frequency that leads to the spin inversion. The spin inversion makes the NMR effect two times larger, however, it needs higher rf magnetic field than that in the depolarization method.

The β -NQR system described in this thesis was designed to meet the criteria listed above. The system is an upgrade of the previous β -NMR system at the NSCL. It has a multi rf capability, utilizing four function generators to produce four different transition frequencies. A 250 W rf amplifier is used to achieve the high magnetic field for spin manipulation. A LCR circuit is used to match the output impedance of the amplifier. A high voltage drop will exist in the LCR circuit and the individual components of this circuit were chosen to be capable of handling high voltages. All the

variable vacuum capacitors can handle high voltage up to ~ 5 kV and are remotely tunable by a stepper motor controlling system. Vacuum relay switches are used to select the capacitors depending applied frequency to realize highest quadrupole moment for LCR circuit. The vacuum relay switches are able to handle high voltages. The response time of the relay switches are fast, (few milliseconds) and in an acceptable limits comparing with the life-time of the exotic nuclei of interest. The resistor, capacitors, switches are all contained in an rf box. All variable functions of the rf box and function generators are remotely controllable.

The complete β -NQR system was tested at high power (58 dB amplification). No rf leaks were observed. The maximum field at the rf coil was ~ 18 G for 700 and 1200 kHz testing frequencies.

The minimum capacitance of the system was measured as 270 pF indicating that the maximum resonance frequency is limited to 2100 kHz at the present conditions. Minimum resonance frequency of 370 kHz was achieved by combining two 4000 pF capacitors.

The first application of the new β -NQR system will be to measure the quadrupole moments of the neutron deficient odd- A K isotopes. The physics goal is to find evidence for low binding of the valence proton in $^{35,37}\text{K}$. The quadrupole moment measurement can provide direct information as the radial charge distribution of these nuclei.

In these proposed experiments, ^{36}Ar primary beam with an energy of 150 MeV/A and ^9B production target with the thickness of 564 mg/cm^2 will be used. The charge pickup reaction produces both ^{37}K and ^{35}K nuclei are produced by charge pickup reaction followed by two neutron evaporations. A KDP single crystals will be used as the host crystal and β -count rates of ^{37}K and ^{35}K are expected as 350 pps/pnA and 5 pps/pnA, respectively.

Bibliography

- [1] V. Kello and A. J. Sadlej. *Chemical. Physics. Letters.*, **292**:403, 1998.
- [2] N. J. Stone. *At. Data and Nucl. Data Tables*, **90**:75, 2005.
- [3] J. E. Kammeraad and L. D. Knutson. *Nucl. Phys. A*, **435**:502, 1985.
- [4] H. F. Schaefer *et al.* *Phys. Rev.*, **181**:181, 1969.
- [5] N. A. Jelly. *Fundamentals of nuclear physics*. University of Cambridge, Cambridge, 1990.
- [6] T. Minamisono *et al.* *Phys. Rev. Lett.*, **69**:2058, 1992.
- [7] M. Fukuda *et al.* *Nucl. Phys. A*, **656**:209, 1999.
- [8] W. A. Hardy *et al.* *Phys. Rev.*, **92**:1532, 1953.
- [9] K. Asahi *et al.* *Phys. Lett. B*, **251**:488, 1990.
- [10] G. A. Souliotis *et al.* *Phys. Rev. C*, **46**:1383, 1992.
- [11] D. E. Groh *et al.* *Phys. Rev. Lett.*, **90**:202502–1, 2003.
- [12] T. D. Lee and C. N. Yano. *Phys. Rev.*, **104**:254, 1956.
- [13] B. A. Brown *et al.* MSU computer code oxbash. Cyclotron Laboratory Report 524, MSU, 1986.
- [14] H. Ogawa *et al.* *Phys. Rev. C*, **67**:064308–1, 2003.
- [15] J. A. Behr *et al.* *Phys. Rev. Lett.*, **79**:375, 1997.
- [16] R. M. Sternheimer and R. F. Peiris. *Phys. Rev. A*, **3**:837, 1971.
- [17] R. W. Schmieder and A. Lurio. *Phys. Rev.*, **173**:76, 1968.
- [18] P. A. Bonczyk and V. W. Hughes. *Phys. Rev.*, **161**:15, 1967.
- [19] Masato Morita. *Beta Decay and Muon Capture*. W. A. Benjamin, INC., Massachusetts, 1973.
- [20] C. R. Sun and B. T. Wright. *Phys. Rev.*, **109**:109, 1958.

- [21] J. Seliger and V. Zager. *Phys. Rev. B*, **49**:14918, 1994.
- [22] C. Slatter. *J. Chem. Phys.*, **9**:16, 1941.
- [23] O. Sundholm and J. Olsen. **98**:7152, 1993.
- [24] T. J. Mertzimekis *et al.* *Phys. Rev. C*, **73**:024318, 2006.

MICHIGAN STATE UNIVERSITY LIBRARIES



3 1293 02845 7749